

Black Hole Hair from Scalar Dark Matter

Lam Hui,^a Daniel Kabat,^b Xinyu Li,^a Luca Santoni,^a Sam S. C. Wong^a

^aDepartment of Physics, Center for Theoretical Physics, Columbia University, 538 West 120th Street, New York, NY 10027, U.S.A.

^bDepartment of Physics and Astronomy, Lehman College, City University of New York, Bronx NY 10468, USA

E-mail: lh399@columbia.edu, daniel.kabat@lehman.cuny.edu,
xinyu.li@columbia.edu, ls3598@columbia.edu, sw3266@columbia.edu

Abstract. We show that a black hole surrounded by scalar dark matter develops scalar hair. This is the generalization of a phenomenon pointed out by Jacobson [1], that a minimally coupled scalar with a non-trivial time dependence far away from the black hole would endow the black hole with hair. In our case, the time dependence arises from the oscillation of a scalar field with a non-zero mass. We systematically explore the scalar profile around the black hole for different scalar masses. In the small mass limit, the scalar field has a $1/r$ component at large radius r , consistent with Jacobson's result. In the large mass limit (with the Compton wavelength of order of the horizon or smaller), the scalar field has a $1/r^{3/4}$ profile yielding a pile-up close to the horizon, while distinctive nodes occur for intermediate masses. Thus, the dark matter profile around a black hole, while challenging to measure, contains information about the dark matter particle mass. As an application, we consider the case of the supermassive black hole at the center of M87, recently imaged by the Event Horizon Telescope. Its horizon size is roughly the Compton wavelength of a scalar particle of mass 10^{-20} eV. We consider the implications of the expected scalar pile-up close to the horizon, for fuzzy dark matter at a mass of 10^{-20} eV or below.

Contents

1	Introduction	1
2	Scalar Profile in the Schwarzschild region ($r < r_i$)	4
3	Outside the sphere of impact ($r > r_i$)	14
3.1	Modified metric and matching	14
3.2	Transmission and reflection coefficients	16
3.3	Field profile	16
3.4	Energy accretion rate	19
4	Discussion	20
A	Scalar wave equation in Schwarzschild geometry	25
B	Asymptotics for $l = \bar{k} = 0$	27
C	Energy density and flux	30

1 Introduction

Like all no-go theorems, the well known no-scalar-hair theorem of Bekenstein [2] can be violated—the theorem is correct of course, but its assumptions can be circumvented. Among the assumptions that go into the theorem, an important one is that the scalar field vanishes far away from the black hole. Jacobson [1] pointed out that, in the case of a massless, minimally coupled scalar, giving the scalar field far away a linear time-dependence is sufficient to generate hair for the black hole.¹ In other words, in a Schwarzschild background,²

$$ds^2 = - \left(1 - \frac{r_s}{r}\right) dt^2 + \left(1 - \frac{r_s}{r}\right)^{-1} dr^2 + r^2 d\theta^2 + r^2 \sin^2 \theta d\phi^2, \quad (1.1)$$

where $r_s \equiv 2GM_{\text{BH}}$ is the Schwarzschild radius (M_{BH} being the black hole mass and G being the Newton constant), Jacobson showed that the equation $\square\phi = 0$ has, in addition to the trivial solution $\phi = 0$ (which would be consistent with Bekenstein’s theorem), a solution of the following form for the scalar ϕ :

$$\phi \propto \left(t + r_s \log\left(1 - \frac{r_s}{r}\right)\right). \quad (1.2)$$

At large r , this asymptotes to t plus a $-r_s^2/r$ tail. In other words, ϕ does not vanish at spatial infinity but rather takes on a linear time dependence. The coefficient of the $1/r$ tail can be interpreted as the scalar charge of the black hole. A non-trivial aspect of this solution

¹For alternative ways to circumvent Bekenstein’s theorem, see for example [3–9] and the review [10]. For an extension of the no-scalar-hair theorem to the galileon, see [11].

²Jacobson also derived the analogous result in a Kerr background. We focused on the non-rotating case in this paper.

is that it is regular at the horizon, which is easiest to see by noting that at the horizon $t + r_*$ (often called v , the Eddington-Finkelstein time) is regular, where r_* is the tortoise coordinate $r_* \equiv r + r_s \log(r/r_s - 1)$. The scalar field ϕ is finite at the horizon, and so is $\partial_\alpha \phi \partial^\alpha \phi$.

The coefficient of the $1/r$ tail is often identified as the scalar charge of the black hole, much like the coefficient of the $1/r$ tail in the gravitational potential is identified as the mass of the black hole.³ In this paper, we take a more general view of what constitutes the scalar hair of a black hole: it needs not have a $1/r$ spatial profile; any non-trivial spatial profile around the black hole is potentially interesting from an observational point of view.

Jacobson’s insight is that a black hole can be endowed with a scalar charge (or scalar hair) by imposing the boundary condition that the scalar has a non-zero time derivative far away from the black hole. The original motivation of Jacobson was to apply this to a cosmologically evolving scalar, in which case the proportionality constant in Eq. (1.2) is set by the Hubble expansion rate H . Given the vast disparity in scale between r_s and $1/H$, this can be interpreted as a very small scalar charge (or very small charge to black hole mass ratio).

This raises an obvious question: how about cases where the time derivative far away from the black hole is much larger? A natural setting for this is a scalar with a non-zero mass, which thus oscillates in time. An appealing scenario is one where dark matter is comprised of such a scalar, which inevitably surrounds the black hole. The question we wish to address in this paper is: *what scalar profile should we expect around a black hole embedded within a dark matter halo made out of a scalar field with non-vanishing mass?* A natural candidate for scalar dark matter is an axion or axion-like-particle. Possible masses range from 10^{-22} eV to 10^{-3} eV [12–25]. The QCD axion tends to occupy the higher mass range, while axions in string theory can span the whole range. At the lowest mass end is what is sometimes referred as fuzzy dark matter [19, 24–29]. Our goal in this paper is to work out the scalar profile for the full range of possible scalar masses.

Addressing the question of interest requires revisiting the massive Klein-Gordon equation in a Schwarzschild background. It is not surprising there is a large literature on this subject. For instance, the solution to the Klein-Gordon equation, in certain limiting cases such as large or small radius, was given by Unruh [30] and Detweiler [31]. The former focused on computing the absorption cross section of the scalar by the black hole, while the latter emphasized the instability associated with super-radiance. More recently, it was pointed out that the exact solutions of the Regge-Wheeler equation and Klein-Gordon equation in Schwarzschild space-time is a special function known as the confluent Heun function [32–35]. A number of authors [36, 37] used the confluent Heun function to compute the quasi-normal spectrum, highlighting in particular the long-lived modes. Related to our discussion are papers on the effect of dark matter on binary inspiral (e.g. [38]), and the Jacobson effect due to a black hole moving in an inhomogeneous scalar background, pointed out by Horbatsch and Burgess [39]. Building on the prior work, our goal in this paper is a rather modest one: we use the exact Heun solution to explore the full range of masses, and frame the discussion in terms of scalar hair à la Jacobson.

It is also worth mentioning there is a large literature on super-radiance around black holes

³To be more precise, one could for instance define the scalar charge to be $Q \equiv \mathcal{C} r_s^2 M_{\text{Pl}}$, where \mathcal{C} is the proportionality constant in $\phi = \mathcal{C}(t + r_s \log[1 - r_s/r])$, and $M_{\text{Pl}} = 1/G$. In this way, Q has mass dimension. We will not need this (somewhat arbitrary) definition in the rest of paper.

[23, 40–42]. The super-radiance cloud can be quantum mechanically generated (when the relevant Compton wavelength is around the horizon size of a rotating black hole), and needs not be related to dark matter.

To set the stage we discuss the scales relevant to our problem. First, there is the Schwarzschild radius r_s :

$$r_s = 2.95 \text{ km} \left(\frac{M_{\text{BH}}}{M_{\odot}} \right). \quad (1.3)$$

Interesting values for r_s range from ~ 30 km for typical LIGO black holes [43], to $\sim 10^7$ km for LISA black holes [44, 45], to 10^{10} km for pulsar timing array PTA black holes [46, 47].⁴ The scales of 10^7 km and 10^{10} km are also roughly the size of the black hole at the center of the Milky Way and that in M87, relevant for the Event Horizon Telescope EHT [48].

We are interested in how this scale compares to the Compton wavelength $1/m$.⁵ Alternatively, we compare the scalar mass m against $1/r_s$, expressed in eV:

$$r_s^{-1} = 6.7 \times 10^{-11} \text{ eV} \left(\frac{M_{\odot}}{M_{\text{BH}}} \right). \quad (1.4)$$

Thus, $1/r_s$ ranges from $\sim 10^{-11}$ eV for LIGO black holes to $\sim 10^{-17}$ eV for LISA black holes to $\sim 10^{-20}$ eV for PTA black holes.

While the background geometry is well described by the Schwarzschild metric close enough to the black hole, sufficiently far from it the gravitational influence of the surrounding matter is non-negligible. We define a scale r_i —we call it the radius of sphere of impact—as the radius within which the black hole dominates the geometry.⁶ In other words, we define $r_s/r_i \equiv v_{\text{typical}}^2$ ($c = 1$), where v_{typical} is the typical velocity dispersion of the surrounding matter (motivated by virial theorem) i.e.⁷

$$\frac{r_s}{r_i} = 10^{-6} \left(\frac{v_{\text{typical}}}{300 \text{ km/s}} \right)^2. \quad (1.5)$$

In realistic settings, r_s/r_i can range from $\sim 10^{-8}$ to $\sim 10^{-5}$. We assume the backreaction of the scalar on the Schwarzschild geometry is negligible for $r < r_i$. We will check below that this is a self-consistent assumption, once we work out the scalar profile.

Our main goal in this paper is to understand the dependence of the scalar profile on the scalar mass m . As we will see, there are 4 different regimes, delineated by 3 different scales: regime I — $m < r_s^{-1}(r_s/r_i)^2$, regime II — $r_s^{-1}(r_s/r_i)^2 < m < r_s^{-1}\sqrt{r_s/r_i}$, regime III — $r_s^{-1}\sqrt{r_s/r_i} < m < r_s^{-1}$, and regime IV — $r_s^{-1} < m$. As we scan the regimes from low to high scalar mass, we go from the wave limit to the particle limit. Typical values for these scales are given in Fig. 1.

⁴All experiments LIGO, LISA and PTA are of course sensitive to a range of black hole masses. See [43–47] for details.

⁵The Compton wavelength is $1/m = 1.97 \text{ km} (10^{-10} \text{ eV}/m)$. Note that the Planck constant \hbar and the speed of light c are set to unity by default.

⁶In the literature, the term radius of sphere of influence is often used to describe the radius within which the black hole’s mass dominates over the mass of the enclosed, surrounding matter. Our r_i coincides with that definition, if v_{typical} is chosen to be the dynamical velocity associated with enclosed matter mass.

⁷In this paper, we by default set the speed of light to unity, and thus v_{typical} should strictly speaking be dimensionless. We restore dimension to v_{typical} to ease comparisons with typical astrophysical velocities.

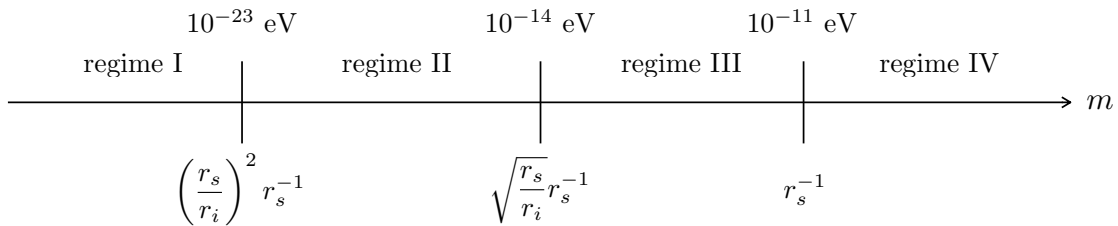


Figure 1: The three mass scales that delineate different regimes in the scalar profile. The ratio r_s/r_i is assumed to be 10^{-6} . The black hole mass is assumed to be about $10M_\odot$, relevant for typical LIGO events. Multiply all numbers by about a factor of 10^{-6} for typical LISA black holes (or for the black hole at the center of the Milky Way); multiply all by a factor of $\sim 10^{-9}$ for typical PTA black holes (or for the black hole at the center of M87).

The organization of the paper is as follows. In Sec. 2, we examine the scalar profile in a Schwarzschild background, exploring different relevant limits of the confluent Heun function. In Sec. 3, we introduce a toy model for the metric at distances outside the radius of sphere of impact r_i . This allows us to connect in a simple way the problem of computing the scalar profile to the problem of scattering. The results of the scattering computation are summarized in Sec. 3. In this paper, we largely focus on s-waves i.e. the accreting scalar having no angular momentum. We discuss in Sec. 4 and App. A under what condition this is a good approximation, and which results are modified or remain the same when angular momentum is included. We conclude in Sec. 4. As an example, we apply our results to the supermassive black hole in M87, and consider the implications for fuzzy dark matter whose Compton wavelength is not much larger than the horizon of the black hole. Certain technical details are relegated to the Appendices: results for non-zero angular momentum are discussed in Appendix A, asymptotics of the Heun function are worked out in Appendix B, and expressions for the energy-momentum tensor can be found in C.

Conventions: For the rest of the paper, we will set $r_s = 2GM_{\text{BH}} = 1$ and restore it when needed for the sake of clarity. In other words, whenever the dimension of a quantity does not match the expected one, the reader can simply put in suitable powers of r_s to recover the correct dimension. We denote $M_{\text{Pl}} = G^{-1/2}$ the standard Planck mass.

Note added: As this manuscript was under preparation, a recent paper by Wong, Davis and Gregory [49] appeared which has some overlap with our work, in particular regarding the scalar charge in the small mass regime. Independently, Clough, Ferreira and Lagos [50] explored the same subject we investigate in this paper – hair associated with a black hole in an oscillating scalar background – using numerical methods that enabled them to include the effects of back-reaction on the solution.

2 Scalar Profile in the Schwarzschild region ($r < r_i$)

We consider a scalar field ϕ of mass m in the Schwarzschild geometry (1.1). For simplicity we set the Schwarzschild radius $r_s = 1$, though it will be restored in a few key expressions. Our focus will be on spherically-symmetric field configurations. This is particularly relevant

for small scalar masses, as we show in section 4 where we discuss the effects of angular momentum. A general discussion of the Klein Gordon equation $(\nabla_\mu \nabla^\mu - m^2) \phi = 0$, including angular momentum, can be found in appendix A.

Restricting to s-waves the Klein-Gordon equation can be expressed in several different ways. For instance:

$$\left[-\partial_t^2 - m^2 \left(1 - \frac{1}{r}\right) + \left(1 - \frac{1}{r}\right)^2 \partial_r^2 + \frac{2}{r} \left(1 - \frac{1}{r}\right) \left(1 - \frac{1}{2r}\right) \partial_r \right] \phi = 0, \quad (2.1)$$

or

$$\left[\partial_t^2 - \partial_{r_*}^2 + m^2 - \frac{m^2}{r} + \frac{1}{r^3} - \frac{1}{r^4} \right] (r\phi) = 0, \quad (2.2)$$

where r_* is the tortoise coordinate defined by $r_* \equiv r + \log(r - 1)$. The second form of the equation is convenient for thinking of the problem as a scattering problem, a perspective we will develop more fully in the next section.

We seek a spherically symmetric solution $\phi(t, r)$ whose time dependence is completely captured by $e^{-i\omega t}$:

$$\phi(t, r) \propto e^{-i\omega t}. \quad (2.3)$$

The most general solution would involve a superposition of different frequencies ω , but we will not need that for the problem at hand. Eq. (2.1) admits the following general solution in terms of the confluent Heun function [34, 35]:

$$\begin{aligned} \phi(t, r) = & c_1 e^{-i\omega t} (r - 1)^{i\omega} e^{i\bar{k}r} \text{HeunC}(-2i\bar{k}, 2i\omega, 0, -\omega^2 - \bar{k}^2, \omega^2 + \bar{k}^2, 1 - r) \\ & + c_2 e^{-i\omega t} (r - 1)^{-i\omega} e^{-i\bar{k}r} \text{HeunC}(2i\bar{k}, -2i\omega, 0, -\omega^2 - \bar{k}^2, \omega^2 + \bar{k}^2, 1 - r), \end{aligned} \quad (2.4)$$

where c_1 and c_2 are constants, and the radial momentum \bar{k} is defined by:⁸

$$\omega = +\sqrt{\bar{k}^2 + m^2}. \quad (2.5)$$

In the non-relativistic limit \bar{k} is related to the energy of the particles by

$$E = \omega - m = \frac{\bar{k}^2}{2m} \quad (2.6)$$

Note that a bound state $E < 0$ corresponds to imaginary \bar{k} .

Although (2.4) is the general solution, it is not a particularly transparent formula. So in what follows we will develop approximations which are valid in different mass ranges. To gain some intuition before proceeding it is useful to return to the differential equation (2.2) and recast it in the form

$$\left(-\partial_{r_*}^2 - \frac{m^2}{r} + \frac{1}{r^3} - \frac{1}{r^4} \right) R = \bar{k}^2 R. \quad (2.7)$$

⁸Note that \bar{k} is the momentum the particle would have at infinity in the Schwarzschild geometry. We are denoting it \bar{k} to distinguish it from k , the typical momentum the particle would have within the galaxy, which we will introduce later. Note also $\text{HeunC}(\alpha, \beta, \gamma, \delta, \eta, z) = \exp(-z\alpha) \text{HeunC}(-\alpha, \beta, \gamma, \delta, \eta, z)$, so the sign of \bar{k} does not matter.

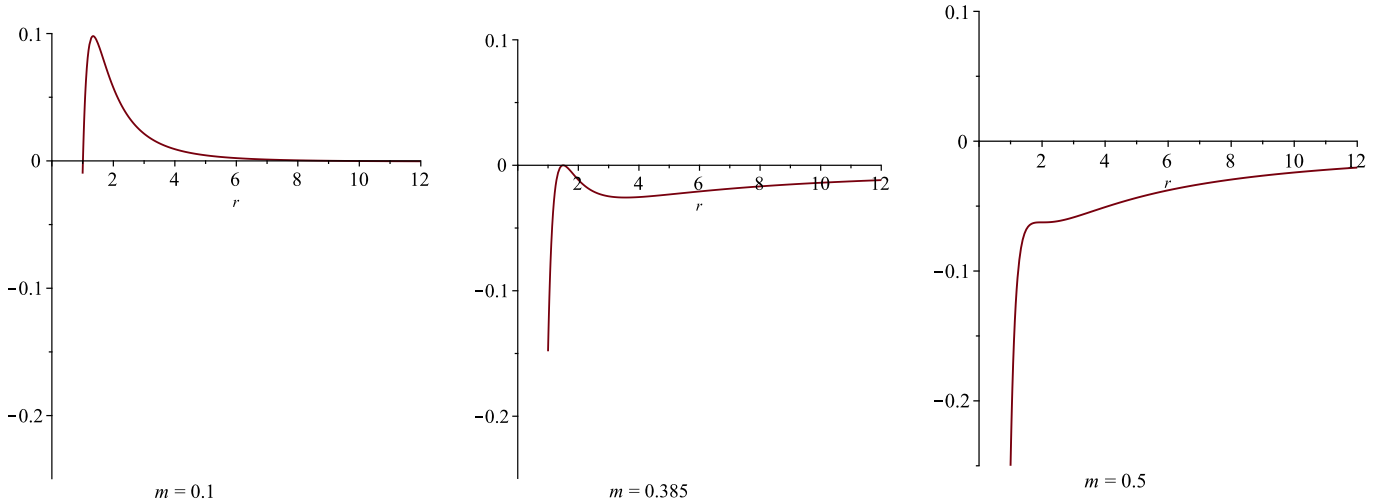


Figure 2: The effective potential $-\frac{m^2}{r} + \frac{1}{r^3} - \frac{1}{r^4}$ in the region outside the horizon $r > 1$, plotted for three different values of m . From left to right $m = 0.1, 0.385, 0.5$.

Here we are setting $\phi(t, r) = e^{-i\omega t} \frac{1}{r} R(r)$. This resembles a Schrödinger equation in a potential $-\frac{m^2}{r} + \frac{1}{r^3} - \frac{1}{r^4}$ that is shown Fig. 2. If m is small there is an $\mathcal{O}(1)$ potential barrier around the unstable maximum at $r \approx \frac{4}{3}$. As m increases the barrier comes down. When $m = \frac{2}{3\sqrt{3}} \approx 0.385$ the top of the barrier is at zero, and for large m the potential is purely attractive. The physics is then pretty clear. At large radius a wave could be coming in from the right. For small m and sufficiently low energy the incoming wave will reflect off the barrier, with a small probability of tunneling into the black hole. But if m (or the energy) is large enough the incoming wave will be almost completely absorbed by the black hole. The black hole itself corresponds to a boundary condition, namely that at the horizon $r \rightarrow 1$ the wave must be purely ingoing (into the horizon).

Now let us return to the general solution (2.4). The definition and properties of the confluent Heun function HeunC are given in appendix B. In the near-horizon limit $r \rightarrow 1$, HeunC approaches unity. Thus, the constant c_1 should be set to zero, so that ϕ is purely ingoing at the horizon i.e.

$$\phi(t, r) \stackrel{r \rightarrow 1}{\approx} c_2 e^{-i\omega(t+r_*)} e^{i(\omega - \bar{k})}. \quad (2.8)$$

In other words, from now on, we consider:

$$\phi(t, r) = c_2 e^{-i\omega t} (r-1)^{-i\omega} e^{-i\bar{k}r} \text{HeunC}(2i\bar{k}, -2i\omega, 0, -\omega^2 - \bar{k}^2, \omega^2 + \bar{k}^2, 1-r), \quad (2.9)$$

where c_2 is an integration constant whose size will be determined by the dark matter density far away from the black hole.

We are interested in particles that are gravitationally bound within the galaxy but have a small binding energy $E < 0$. That is, we are interested in ω slightly smaller than m . For simplicity to capture the relevant physics we will focus on the marginally-bound case $\omega = m$. From (2.7) this should be a reasonable approximation as long as \bar{k}^2 is small compared to the potential, $|\bar{k}|^2 < m^2/r_i$. So we set $\omega = m$ and $\bar{k} = 0$ and take

$$\phi(t, r) = c_2 e^{-im(t+\log(r-1))} \text{HeunC}(0, -2im, 0, -m^2, m^2, 1-r). \quad (2.10)$$

Note that for the sake of generality we are allowing ϕ to be complex. However for many applications ϕ is real (e.g. if ϕ is the angular field corresponding to an axionic degree of freedom). To treat the two cases in parallel we adopt the convention that a real solution can be obtained from a complex solution by adding the complex conjugate. So for example we take the real field corresponding to (2.10) to be

$$\phi(t, r) = c_2 e^{-im(t+\log(r-1))} \text{HeunC}(0, -2im, 0, -m^2, m^2, 1-r) + \text{c.c.}, \quad (2.11)$$

where c.c. stands for complex conjugation. This convention fixes the relative normalization of what we mean by c_2 in the real and complex cases. It is a useful convention for reasons we turn to next. *For the most part, the fields below are given for a complex field ϕ , but it is simply a matter of adding the complex conjugate if one is interested in a real scalar ϕ .*

Before proceeding let us discuss our procedure for normalizing the field amplitude. It is convenient to fix the normalization in terms of a physical observable, namely the energy density of the scalar field ρ_i evaluated at a radius r_i which is much larger than the Schwarzschild radius. We have in mind that r_i is the radius of the sphere of impact; see the discussion around (1.5) for a precise definition of this quantity. First consider a complex scalar field. To evaluate the energy density we use the stress tensor given in appendix C. Far from the black hole (so that the geometry is approximately flat) and neglecting spatial gradients (as appropriate for non-relativistic particles) the energy density of a complex scalar field is

$$\rho = T^{tt} \approx |\partial_t \phi|^2 + m^2 |\phi|^2 \approx 2m^2 |\phi|^2, \quad (2.12)$$

where we assumed $\omega \approx m$. Thus for a complex scalar field we fix the field amplitude by setting

$$\rho_i = 2m^2 |\phi(r = r_i)|^2. \quad (2.13)$$

Now let us consider a real scalar field. Given a complex scalar $\phi = Ae^{-imt}$ where A is a real amplitude, we would build a real scalar field by setting $\phi = Ae^{-imt} + \text{c.c.} = 2A \cos mt$. For a real scalar the energy density has a factor of 1/2,

$$\rho \approx \frac{1}{2} (\dot{\phi}^2 + m^2 \phi^2) = 2m^2 A^2. \quad (2.14)$$

This means the real scalar field we build by adding the complex conjugate has exactly the same energy density as the complex scalar we started from. *Below we will write formulas for complex fields, normalized by their energy density ρ_i . To obtain a real field merely add the complex conjugate to the expressions below; ρ_i will be the energy density of the real scalar field at r_i .*

So far we have found the exact solution (2.10), which near the horizon becomes an ingoing wave

$$\phi(t, r) = c_2 e^{-im(t+\log(r-1))} \quad \text{as } r \rightarrow 1. \quad (2.15)$$

Now let us consider the large r behavior of $\phi(t, r)$. The large r limit of the confluent Heun function (with $\bar{k} = 0$) is derived in appendix A and implies⁹

$$\begin{aligned} \phi(t, r) = & c_3 e^{-imt} \frac{1}{r^{3/4}} e^{2im\sqrt{r}} \left(1 + \mathcal{O}\left(\frac{1}{m\sqrt{r}}\right) \right) \\ & + c_4 e^{-imt} \frac{1}{r^{3/4}} e^{-2im\sqrt{r}} \left(1 + \mathcal{O}\left(\frac{1}{m\sqrt{r}}\right) \right), \end{aligned} \quad (2.16)$$

⁹Note that the large r behavior for a non-zero \bar{k} is quite different. See Eq. (A.14).

where c_3 and c_4 are constants related to c_2 (the precise relations to be given below). This has a simple interpretation, that c_3 is the coefficient of an outgoing wave and c_4 is the coefficient of an ingoing wave. This is a good approximation as long as $m\sqrt{r} \gg 1$. In other words, this is not simply a large r expansion, but rather a large $m\sqrt{r}$ expansion. Restoring r_s , the expansion is valid for $m \gg 1/\sqrt{rr_s}$. The reader might wonder where the $r^{-3/4}$ behavior comes from, and why there is a \sqrt{r} in the exponent: an intuitive explanation is given in Sec. 4. An expression like Eq. (2.16), while strictly valid only for $m \gg 1/\sqrt{r}$, will be treated as an acceptable approximation for $m \gtrsim 1/\sqrt{r}$ with the understanding that when m approaches $1/\sqrt{r}$, there would be order one corrections.

We now summarize the behavior of the field in different regimes. To start suppose the mass is such that the combination $m\sqrt{r_i}$ is large, where r_i is the radius of the sphere of impact. In this case the field near r_i is described by (2.16). This large $m\sqrt{r_i}$ limit can be further divided into two separate regimes. One is where the mass is so large that $m \gtrsim 1$. In this case, which we call regime IV, there is no potential barrier around the black hole as can be seen in the right panel of Fig. 2. Thus we expect to have an ingoing wave everywhere. Indeed the relevant approximation for the Heun function is given in (B.17). It implies that the large- r behavior is given by setting $c_3 \approx 0$ and $c_4 \approx c_2$ in (2.16), and that (2.16) is in fact a good approximation as long as $r \gtrsim r_s$. Very close to the horizon we still have the near-horizon behavior (2.15). That is,

$$\begin{aligned} \text{Regime IV : } m \gtrsim r_s^{-1} \\ \phi(t, r) \approx \sqrt{\frac{\rho_i}{2m^2}} \left(\frac{r_i}{r}\right)^{3/4} e^{-imt} e^{-i2m\sqrt{rr_s}} \quad \text{for } r_s \lesssim r < r_i, \\ \phi(t, r) \approx c_2 e^{-im(t+r_*)} e^{imr_s} \quad \text{where } c_2 \approx \sqrt{\frac{\rho_i}{2m^2}} \left(\frac{r_i}{r_s}\right)^{3/4} \quad \text{for } r \rightarrow r_s, \end{aligned} \quad (2.17)$$

where r_s is restored for clarity. We fixed the normalization of ϕ by setting the energy density to be ρ_i at $r = r_i$. The large r expression is strictly correct only for $r \gg r_s$ but is in practice a reasonable approximation down to $r \gtrsim r_s$. Thus the amplitude at the horizon c_2 is given by extrapolating the large r expression to $r = r_s$.

Next we consider the case where $m \lesssim 1$, while $m \gtrsim 1/\sqrt{r_i}$ continues to hold. In this case, which we refer to as regime III, the field near r_i is well-described by (2.16). Thus we have ingoing and outgoing waves near the sphere of impact. However since $m \lesssim 1$ there is a significant potential barrier near the black hole, as seen in the left panel of Fig. 2, and we expect the ingoing wave to reflect off the barrier. That is, we expect c_3 and c_4 to have roughly the same magnitude. This means a standing wave will develop around the black hole. The relevant approximation is given in (B.14) and implies, restoring r_s for clarity:

$$\begin{aligned}
&\text{Regime III : } (r_i r_s)^{-1/2} \lesssim m \lesssim r_s^{-1} \\
&\phi(t, r) \approx \sqrt{\frac{\rho_i}{m^2}} \left(\frac{r_i}{r}\right)^{3/4} e^{-imt} \cos(2m\sqrt{rr_s} - 3\pi/4) \quad \text{for } m^{-2}r_s^{-1} \lesssim r < r_i, \\
&\phi(t, r) \approx c_2 e^{-im(t+r_*-r)} \quad \text{where } c_2 \approx \sqrt{\frac{\rho_i}{m^2}} \left(\frac{r_i}{m^{-2}r_s^{-1}}\right)^{3/4} \sqrt{\pi} \quad \text{for } r_s < r \lesssim m^{-2}r_s^{-1}.
\end{aligned} \tag{2.18}$$

Note that the energy density ρ oscillates in space like $[\cos(2m\sqrt{rr_s} - 3\pi/4)]^2$; the quantity ρ_i is not necessarily the density at precisely r_i , but is rather the density averaged over an oscillation cycle around r_i i.e. replacing the $[\cos]^2$ by $1/2$. As explained in the appendix, this result is obtained assuming $m \ll 1$, but it gives a reasonable approximation as long as $m \lesssim 1$. A noteworthy point about the profile in regime III: aside from the oscillations which pile up against the horizon, the field is roughly constant from r_s out to $1/m^2 r_s$, then begins to drop off like $1/r^{3/4}$.

Now let us consider what happens when $m \lesssim 1/\sqrt{r_i}$. As shown in Appendix B, the Heun function has an expansion in the small mass limit:¹⁰

$$\text{HeunC}(0, -2im, 0, -m^2, m^2, z) = 1 + im \log(1 - z) + \mathcal{O}(m^2). \tag{2.19}$$

Therefore, in this limit, $\phi(t, r)$ takes the form (see Appendix B):

$$\phi(t, r) = c_2 e^{-imt} \left(1 - im \log(1 - r^{-1}) - \frac{1}{2} m^2 r + \dots \right). \tag{2.20}$$

A few comments are in order about this expression. First of all, we are not displaying all the order m^2 terms in the parentheses; they can be found in Appendix B. We keep the $m^2 r$ term because among the m^2 terms, this dominates at large r . There is a delicate balance here, we are interested in large r , but not so large that $m^2 r \gtrsim 1$, i.e. we are interested in $m^2 r \lesssim 1$, or $m \lesssim 1/\sqrt{r}$, or $r \lesssim 1/m^2$.¹¹ Now, for large r , the logarithm can be expanded to give a term that goes like im/r . Comparing these two terms, we see that whether one dominates over the other is determined by how large m is compared to $1/r^2$, or how big r is compared $1/\sqrt{m}$. There are thus roughly two possibilities. Suppose we are in what we will call regime II: $1/r_i^2 \lesssim m \lesssim 1/\sqrt{r_i}$ —recall that r_i is the largest radius we can go out to before the geometry deviates from Schwarzschild—then, for $1/\sqrt{m} \lesssim r \lesssim r_i$, the field profile is dominated by the $m^2 r$ term¹², but for $1 \lesssim r \lesssim 1/\sqrt{m}$, the field profile is dominated by the logarithm or im/r term. The second possibility is what we will call regime I: $m \lesssim 1/r_i^2$. In this case, the logarithm or im/r term always dominates over the $m^2 r$ term (because $r \lesssim r_i$ to stay within the Schwarzschild geometry). Summarizing, we have, again restoring r_s :

¹⁰Restoring units, this expansion in powers of m is valid if both $mr_s \ll 1$ and – more importantly – if $m\sqrt{rr_s} \ll 1$.

¹¹Note that as long as $m \lesssim 1/\sqrt{r}$, $m \lesssim 1$ is automatic because $r \gtrsim 1$, implying the logarithm term is also small compared to unity. Moreover, $m \lesssim 1/\sqrt{r}$ also implies $m \lesssim r$, consistent again with the fact that the logarithm term is small compared to unity (recall that the logarithm can be expanded to give im/r for large r). In other words Eq. (2.20) can be thought of as a small $m\sqrt{r}$ but large r expansion.

¹²Even in this case, it is useful to keep the logarithm or im/r term because it contributes to the energy flux in a non-trivial way (see below).

$$\begin{aligned}
&\text{Regime II : } r_s/r_i^2 \lesssim m \lesssim 1/\sqrt{r_i r_s} \\
\phi(t, r) &\approx \sqrt{\frac{\rho_i}{2m^2}} e^{-imt} \left(1 + \frac{imr_s^2}{r} - \frac{1}{2} m^2 r r_s \right) \quad \text{for } \sqrt{r_s/m} \lesssim r \lesssim r_i, \\
\phi(t, r) &\approx \sqrt{\frac{\rho_i}{2m^2}} e^{-imt} \left(1 + \frac{imr_s^2}{r} \right) \quad \text{for } r_s \ll r \lesssim \sqrt{r_s/m} \\
\phi(t, r) &\approx c_2 e^{-im(t+r_*)} \quad \text{where } c_2 \approx \sqrt{\frac{\rho_i}{2m^2}} \quad \text{for } r \rightarrow r_s,
\end{aligned} \tag{2.21}$$

and

$$\begin{aligned}
&\text{Regime I : } m \lesssim r_s/r_i^2 \\
\phi(t, r) &\approx \sqrt{\frac{\rho_i}{2m^2}} e^{-imt} \left(1 + \frac{imr_s^2}{r} \right) \quad \text{for } r_s \ll r \lesssim r_i \\
\phi(t, r) &\approx c_2 e^{-im(t+r_*)} \quad \text{where } c_2 \approx \sqrt{\frac{\rho_i}{2m^2}} \quad \text{for } r \rightarrow r_s.
\end{aligned} \tag{2.22}$$

In regime I, which is the extreme small mass limit (or the wave limit), one can make a stronger statement about the scalar profile. Ignoring the order m^2 term in both the spatial and temporal dependence in Eq. (2.20), but without expanding the logarithm, we have (restoring r_s):

$$\phi(t, r) = c_2 \left(1 - im \left[t + r_s \log \left(1 - \frac{r_s}{r} \right) \right] \right). \tag{2.23}$$

The zero order solution $\phi(t, r) = c_2$ is of course the trivial solution to the massless Klein-Gordon equation. The order m solution is in fact the non-trivial solution to the massless Klein-Gordon equation found by Jacobson: $\phi \propto (t + r_s \log(1 - r_s/r))$ (Eq. (1.2)). It is worth emphasizing that this (massless) solution holds at all radii.

It is useful to give an example of what a real scalar field profile looks like. For instance, in regime I, by adding the complex conjugate, one obtains in the radius range $r_s \ll r \lesssim r_i$:

$$\phi(t, r) \approx \sqrt{\frac{2\rho_i}{m^2}} \left(\cos(mt) + \frac{mr_s^2}{r} \sin(mt) \right). \tag{2.24}$$

Note that the time origin is arbitrary; for instance, one could swap the cosine and the sine by shifting t . Note also that by assumption, regime I implies $mr_s \ll 1$ (see Fig. 1) and so the $1/r$ scalar hair is weak. In other words, the scalar field amplitude at the horizon is not too different from the amplitude far away (at r_i). The $1/r$ tail is important for getting the correct energy flux, however, as we will see.¹³

Let us illustrate the different behaviors of the Klein Gordon scalar by some numerical examples. Fig. 3 shows the field as a function of t and r_* for $m = 1$ (roughly regime IV). It

¹³It is also worth emphasizing that this $1/r$ tail was at some level known in much earlier work, see e.g. equation 42 of [30] (also [31]). What we have done here is rather modest—an exploration of the scalar profile or hair as the mass is varied, using properties of the Heun function. The use of the Heun function and its expansion (2.20) also allows us to deduce the $1/r$ tail with the correct coefficient without going through matching procedures.

illustrates the growth of the field near the black hole and the plane wave propagating into the horizon. Fig. 4 shows the real scalar ϕ as a function of t and r_* , for two different masses (in essentially regimes III and regime IV). In Figs. 3 and 4 (and only in those figures) we fixed the field amplitude to be 1 at the horizon, that is, we set $c_2 = 1$. Finally, to see how the amplitude of the field varies with radius for different masses, it is convenient to eliminate the time dependence by time-averaging ϕ^2 over a period of oscillation. The resulting $\overline{\phi^2}$ is shown in Fig. 5. The masses of 1, 1/5 and 1/20 roughly span regimes IV, III and II, and one can see pile-up close to the horizon in IV and III, the standing wave in III and a rather flat profile for II, in agreement with the analytic approximations given above. We should emphasize that all these figures (Figs. 3, 4 and 5) show numerical solutions to the differential equation, obtained using the `HeunC` function in Maple, and do not rely on any approximations.

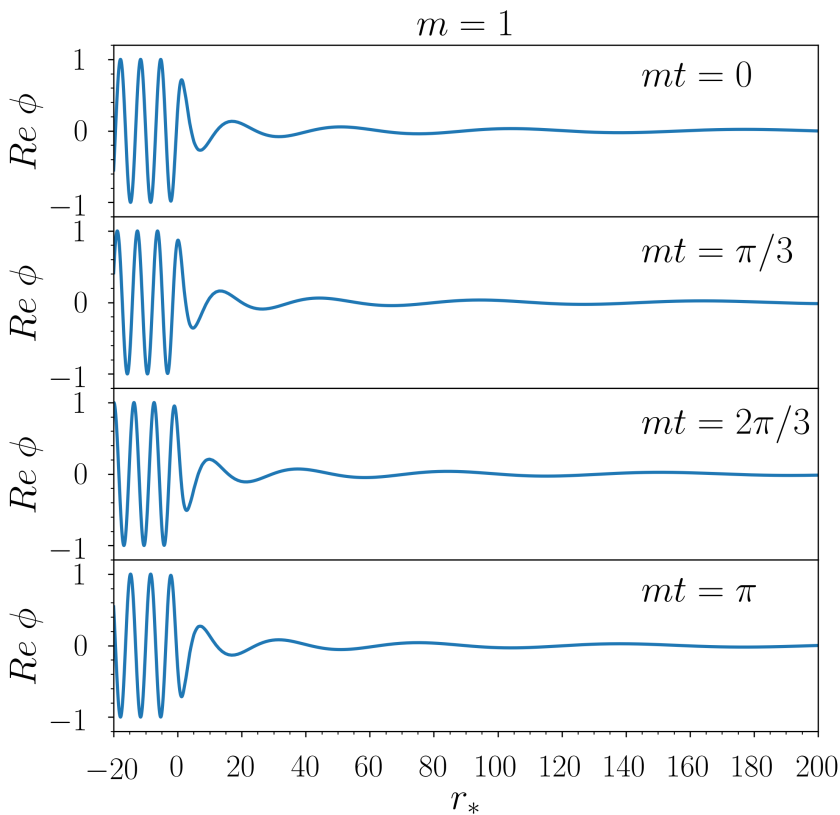


Figure 3: Four snapshots of a real scalar field with $m = 1$ as a function of r_* . These are frames from an animation. To view the video on arXiv.org follow the link under “Ancillary files”. Here ϕ is normalized to unity at the horizon.

Lastly, we conclude this section by computing the energy flux near the horizon. Conservation of energy-momentum can be expressed as

$$\frac{1}{\sqrt{-g}}\partial_\mu(\sqrt{-g}T^\mu{}_\nu) - \frac{1}{2}(\partial_\nu g_{\mu\lambda})T^{\mu\lambda} = 0, \quad (2.25)$$

which uses the fact that the energy-momentum tensor $T^{\mu\lambda}$ is symmetric. Because the

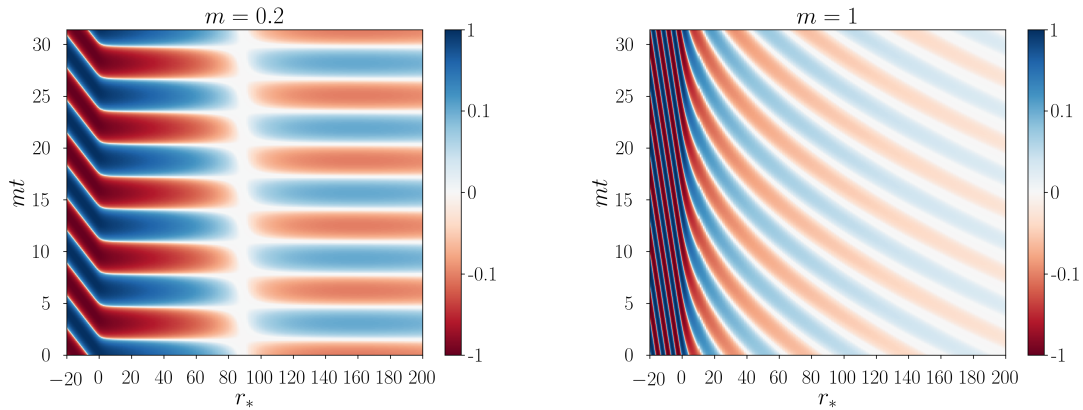


Figure 4: Two massive real scalar fields (left: $m = \frac{1}{5}$; right: $m = 1$) in a pure Schwarzschild geometry ($r_s = 1$), showing ϕ as a function of t and r_* where r_* is the tortoise coordinate. The color scheme shows the scalar field amplitude with the largest positive value as deep blue and the most negative value as deep red. One can see that the scalar field oscillates with a larger amplitude closer to the horizon. At $r_* > 0$, a heavy scalar (regime IV) is purely ingoing due to the vanishing barrier in the potential. At $r_* > 0$, the lighter scalar (regime III) has both ingoing and outgoing waves of comparable amplitudes, hence the standing wave pattern with a node at $r_* \sim 90$. For $r_* < 0$, the potential barrier almost vanishes therefore ϕ becomes purely ingoing plane wave with the speed of light. (We have effectively chosen $r_i \sim 200$ in these illustrations.)

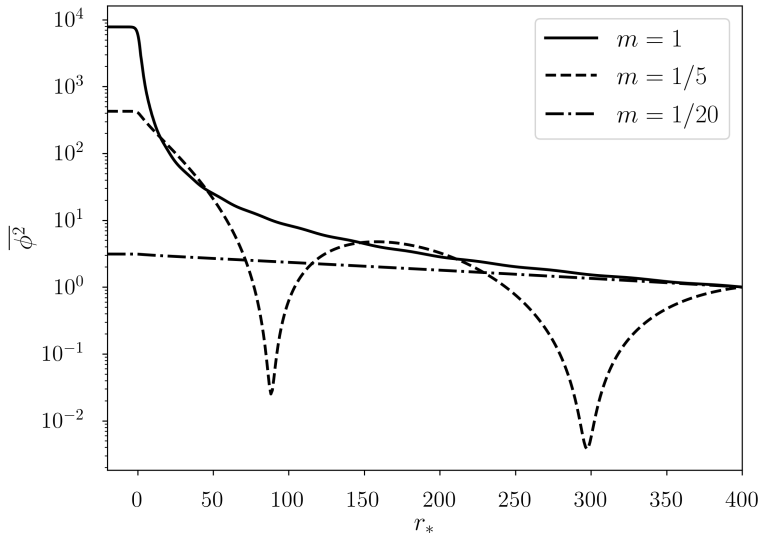


Figure 5: This shows the time-averaged $\overline{\phi^2}$ as a function of the tortoise coordinate r_* in a Schwarzschild geometry with $r_s = 1$. The curves are all normalized to unity at $r_* = 400$ i.e. r_i is effectively chosen to be ~ 400 . The masses of 1, $1/5$ and $1/20$ roughly span regimes IV, III and II.

Schwarzschild metric is time independent, the conservation of energy (for ϕ with only t and r dependence) takes a particularly simple form:

$$\partial_t(r^2 T^t_t) + \partial_r(r^2 T^r_t) = 0. \quad (2.26)$$

The amount of energy flowing inward across a sphere of radius r per unit time is thus

$$\Phi = 4\pi r^2 T^r_t = -4\pi r^2 \left(1 - \frac{1}{r}\right) T^{rt}. \quad (2.27)$$

The energy-momentum tensor is given in (C.2) for a complex scalar and (C.13) for a real scalar. So more explicitly we have

$$\Phi = 4\pi r^2 \left(1 - \frac{1}{r}\right) [\partial_t \phi^* \partial_r \phi + \partial_t \phi \partial_r \phi^*] \quad (2.28)$$

for a complex scalar and

$$\Phi = 4\pi r^2 \left(1 - \frac{1}{r}\right) \partial_t \phi \partial_r \phi \quad (2.29)$$

for a real scalar. For a complex scalar with the $e^{-i\omega t}$ time dependence, it is manifest that both T^t_t and T^r_t would be time-independent. Thus, Eq. (2.26) tells us that Φ should be independent of r . For a real scalar, which would have $\cos(\omega t)$ or $\sin(\omega t)$ time dependence, T^t_t and T^r_t are no longer time independent. However, as long as one averages over a cycle of oscillation, it can be shown that $\partial_t T^t_t = 0$, in which case Eq. (2.26) also tells us the averaged Φ is r independent.

In other words, Φ (or its average) can be computed at any radius r including in particular the horizon. Using expressions in appendix C, and the near-horizon solution Eq. (2.8), we find

$$\Phi = 8\pi\omega^2 |c_2 e^{-i\bar{k}}|^2, \quad (2.30)$$

where we keep ω and \bar{k} general, even though we will mostly be interested in $\omega = m$ and $\bar{k} = 0$. For a real scalar ϕ , with the convention described below (2.11), we have

$$\Phi_{\text{real } \phi} = 16\pi\omega^2 |c_2 e^{-i\bar{k}}|^2 \sin^2 \omega t. \quad (2.31)$$

Note that $c_2 e^{-i\bar{k}}$ in principle has a phase that can enter into the phase of the sine which we ignore because the origin of t is arbitrary in any case. Averaging over time:

$$\text{time averaged } \Phi_{\text{real } \phi} = 8\pi\omega^2 |c_2 e^{-i\bar{k}}|^2. \quad (2.32)$$

At the horizon, it does not seem so crucial that we average over time. But it can be checked easily that at larger radii, it is only the time averaged Φ that is r independent for a real scalar (try for instance computing Φ for Eq. (2.24)).

Given our results for the scalar field it is straightforward to relate the energy accretion rate Φ to the energy density at the sphere of impact ρ_i . Setting $\bar{k} = 0$, so that $\omega = m$ and $\Phi = 8\pi m^2 |c_2|^2$, we find that, as follows from [30],

$$\text{regimes I and II } (m \lesssim 1/\sqrt{r_i r_s}): \quad \Phi = 4\pi r_s^2 \rho_i, \quad (2.33)$$

$$\text{regime III } (1/\sqrt{r_i r_s} \lesssim m \lesssim 1/r_s): \quad \Phi = 2\pi \cdot 4\pi r_s^2 \rho_i \left(\frac{r_i}{m^{-2} r_s^{-1}}\right)^{3/2}, \quad (2.34)$$

$$\text{regime IV } (m \gtrsim 1/r_s): \quad \Phi = 4\pi r_s^2 \rho_i \left(\frac{r_i}{r_s}\right)^{3/2}. \quad (2.35)$$

A few comments on these results are in order. First, in regimes I and II where the mass is small, the field amplitude and hence the energy density is roughly constant from r_i down to the horizon.¹⁴ Near the horizon the field is effectively massless and waves move toward the horizon at the speed of light. To emphasize this point we can restore the speed of light and write the flux in regimes I and II as $\Phi = 4\pi r_s^2 \rho_i c$. In regime III there is an enhancement factor associated with the $1/r^{3/4}$ growth of the field from r_i down to the radius $1/m^2 r_s$ where the growth cuts off. The numerical coefficient in regime III is a bit ambiguous since the energy density oscillates in space; we have adopted the averaging procedure described below (2.18) to get a rough estimate. In regime IV there is enhancement associated with the $1/r^{3/4}$ growth from r_i down to the horizon. The flux in regime IV has an intuitive form when expressed in terms of the virial velocity $v_{\text{typical}} = \sqrt{r_s/r_i}$, namely $\Phi = 4\pi r_i^2 \rho_i v_{\text{typical}}$. That is, the energy density ρ_i flows across the sphere of impact with velocity v_{typical} .

3 Outside the sphere of impact ($r > r_i$)

In the previous section we examined the behavior of a scalar field in a Schwarzschild geometry. This is a reasonable approximation close to the black hole, but breaks down around the sphere of impact where the potential of the surrounding matter takes over. Here we take steps toward modeling a more realistic situation. We will slightly modify the geometry far from the black hole in a way that makes the effective potential constant. This should be viewed as a tractable toy model of a more realistic situation. The toy model has the advantage of giving us incoming and outgoing spherical waves. This makes the analysis and interpretation clean and allows us to connect the black hole hair problem to a standard scattering problem.

Below we first introduce a toy model for the geometry at $r > r_i$. Then we compute the transmission and reflection coefficients for an incoming wave, discuss the scalar field profile, and finally consider the energy accretion rate. We will denote the typical virial velocity $v = \sqrt{r_s/r_i}$. Our main goal will be to understand the dependence on the scalar mass m . As we vary this mass we will hold v fixed, which means the momentum far from the black hole $k = mv$ will scale with m .

3.1 Modified metric and matching

To modify the metric we choose a radius r_i and match the Schwarzschild metric for $r < r_i$ to a constant metric for $r > r_i$. That is, we take

$$ds^2 = \begin{cases} -\left(1 - \frac{1}{r}\right) dt^2 + \left(1 - \frac{1}{r}\right)^{-1} dr^2 + r^2 d\Omega^2 & r < r_i \\ -f_i dt^2 + f_i^{-1} dr^2 + r^2 d\Omega^2 & r > r_i \end{cases} \quad (3.1)$$

where $f_i = 1 - \frac{1}{r_i}$. The metric is continuous across r_i . For $r > r_i$ there is a constant redshift factor and spatial slices have a conical geometry, but the deviation from Minkowski space is small provided $r_i \gg 1$ so that $f_i \approx 1$.¹⁵ As follows from appendix A the tortoise coordinate

¹⁴This is discussed in more detail in section 3.4.

¹⁵Keep in mind that realistically, the metric does not maintain this conical form as one goes to even larger radii, where metric fluctuations of the galaxy comes into play. Our simple toy model is chosen for simplicity rather than realism. It is worth emphasizing that none of the results at $r < r_i$ are affected by the choice of the toy model for what happens at $r > r_i$.

is

$$r_* = \begin{cases} r + \frac{r_i}{r_i-1} + \log \frac{r-1}{r_i-1} & r < r_i \\ \frac{r}{f_i} & r > r_i \end{cases} \quad (3.2)$$

and the effective potential is

$$V = \begin{cases} m^2 - \frac{m^2}{r} + \frac{1}{r^3} - \frac{1}{r^4} & r < r_i \\ m^2 - \frac{m^2}{r_i} & r > r_i \end{cases} \quad (3.3)$$

Note that the effective potential is not quite continuous across r_i . It has a step discontinuity at $r = r_i$, but the step is small and will not have much effect provided $r_i \gg 1$.

In the Schwarzschild region $r < r_i$ we adopt the solution given in (2.9), which is smooth across the future horizon. On the other hand, for $r > r_i$ we have oscillating solutions,

$$\phi(t, r) = e^{-i\omega t} \frac{1}{r} R(r) \quad \text{with} \quad R(r) = b_1 e^{ikr_*} - b_2 e^{-ikr_*}. \quad (3.4)$$

The relative minus sign is conventional for s-wave scattering. In (3.4) the momentum k is real and positive, and it is related to \bar{k} , the momentum at infinity in a pure Schwarzschild geometry, by¹⁶

$$k^2 = \bar{k}^2 + m^2/r_i. \quad (3.5)$$

The solutions (3.4) correspond to spherical waves,

$$\phi(t, r) = e^{-i\omega t} \frac{1}{r} \left(b_1 e^{ikr_*} - b_2 e^{-ikr_*} \right), \quad (3.6)$$

where b_2 and b_1 are the amplitudes of the incoming and reflected waves respectively.

Patching the solutions (2.9) and (3.6) together by requiring that ϕ and $\partial_{r_*}\phi$ are continuous across r_i leads to the system of equations

$$c_2(r_i - 1)^{-i\omega} e^{-i\bar{k}r_i} r_i \text{HeunC} = b_1 e^{ikr_{*i}} - b_2 e^{-ikr_{*i}}, \quad (3.7)$$

$$c_2(r_i - 1)^{-i\omega} e^{-i\bar{k}r_i} f_i \left[\left(1 - \frac{i\omega}{f_i} - i\bar{k}r_i \right) \text{HeunC} - r_i \text{HeunC}' \right] = ik \left(b_1 e^{ikr_{*i}} + b_2 e^{-ikr_{*i}} \right), \quad (3.8)$$

where $\text{HeunC} = \text{HeunC}(2i\bar{k}, -2i\omega, 0, -\omega^2 - \bar{k}^2, \omega^2 + \bar{k}^2, 1 - r_i)$ and HeunC' denotes a derivative with respect to the last argument.

The matching equations (3.7)-(3.8) are somewhat unwieldy but they simplify in various limits. The most interesting situation is a field that oscillates with frequency $\omega = m$, which corresponds to setting $\bar{k} = 0$ and $k = m/\sqrt{r_i}$. Then for small mass and large r_i we can use the expansion (B.6) in App. B to find¹⁷

$$\frac{b_1}{b_2} = 1 - \frac{2m^2}{\sqrt{r_i}} + \frac{i}{3} r_i^{3/2} m^3 + \mathcal{O}(m^4), \quad (3.9)$$

$$\frac{c_2}{b_2} = \frac{2im}{\sqrt{r_i}} - \frac{m^2}{r_i^{5/2}} + i\sqrt{r_i} m^3 + \mathcal{O}(m^4), \quad (3.10)$$

¹⁶Note that in general \bar{k}^2 can be negative as discussed below (2.6).

¹⁷Restoring the Schwarzschild radius r_s , we are expanding in powers of m and taking $r_s \ll r_i \ll 1/m^2 r_s$. The last condition is necessary for the validity of the m expansion.

On the other hand, expanding for large mass and large r_i using (B.17) gives

$$\frac{b_1}{b_2} = \frac{1}{2\sqrt{r_i}} e^{-2im\sqrt{r_i}}, \quad (3.11)$$

$$\frac{c_2}{b_2} = -\frac{1}{r_i^{1/4}} e^{im\sqrt{r_i}}. \quad (3.12)$$

3.2 Transmission and reflection coefficients

We begin by computing the transmission and reflection coefficients for scattering off the black hole. The energy flux across the horizon was given in (2.30). Then, the incoming and outgoing fluxes associated with (3.6) are

$$\Phi_{\text{in}} = 8\pi k\omega |b_2|^2, \quad (3.13)$$

$$\Phi_{\text{out}} = 8\pi k\omega |b_1|^2. \quad (3.14)$$

Thus, the transmission and reflection coefficients take on the form

$$\mathcal{T} = \frac{\omega}{k} \left| \frac{c_2 e^{-i\bar{k}}}{b_2} \right|^2, \quad \mathcal{R} = \left| \frac{b_1}{b_2} \right|^2, \quad (3.15)$$

with $\mathcal{T} + \mathcal{R} = 1$. These are plotted in Fig. 6 as a function of m . As expected, for small mass the wave mostly reflects off the barrier while for large mass it mostly falls into the black hole. This also follows from the expansions (3.9)-(3.12), which imply, for small mass,

$$\mathcal{T} \approx \frac{4m^2}{\sqrt{r_i}}, \quad \mathcal{R} \approx 1 - \frac{4m^2}{\sqrt{r_i}}, \quad (3.16)$$

while, for large mass,

$$\mathcal{T} \approx 1, \quad \mathcal{R} \approx 0. \quad (3.17)$$

3.3 Field profile

In section 2 we explored the field profile near the black hole in various mass regimes. Here we match those results to the spherical waves (3.6) and discuss the behavior of the field at $r > r_i$. To this end, we will set $\bar{k} \approx 0$ so that $\omega \approx m$, and we will take $r_i \gg 1$ in such a way that $f_i \approx 1$. Note that this means $r_* \approx r$ for $r > r_i$. There are basically four situations that occur, which, in order of increasing mass, are given by the following.

- I. In regime I, $m \lesssim 1/r_i^2$ or equivalently $m \lesssim v^4$, the field for $r < r_i$ is given by retaining the first-order term in (2.20),

$$\phi(t, r < r_i) = \sqrt{\frac{\rho_i}{2m^2}} e^{-imt} (1 - im \log(1 - 1/r)) \quad (3.18)$$

where we have normalized as in (2.22). Since the mass is small, i.e. $kr_i = mvr_i \ll 1$, the field does not oscillate on length scales of interest and we can expand the exponentials in (3.6) to first order. Matching the field and its derivative at r_i gives

$$\phi(t, r_i < r < 1/k) = \sqrt{\frac{\rho_i}{2m^2}} e^{-imt} \left(1 + \frac{im}{r} \right). \quad (3.19)$$

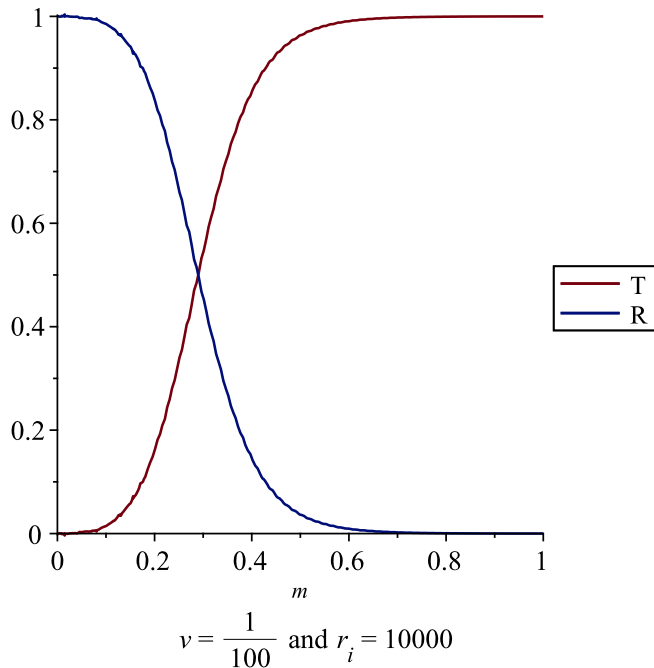


Figure 6: Transmission and reflection coefficients as a function of m .

Note that the homogeneous term dominates and the $1/r$ hair is a small correction. This result also follows from using the small-mass expansion (3.9) to first nontrivial order.

- II. In regime II the mass is larger, $m > v^4$ but $kr_i = mvr_i < 1$. In this regime we can still expand in powers of the mass. But in (2.20) the second-order term is enhanced by a factor of mr^2 compared to the first-order term and can make the dominant correction to the field profile. This means we should retain subleading terms in the small-mass expansion (3.9) – (3.10) and we should expand the exponentials in (3.6) to second order. Carrying out the matching of the field and its derivative at r_i gives

$$\phi(t, 1 < r < r_i) = c_2 e^{-imt} \left(1 + \frac{1}{2} m^2 r_i + \frac{im}{r} - \frac{1}{2} m^2 r + \mathcal{O}(m^3) \right) \quad (3.20)$$

$$\phi(t, r_i < r < 1/k) = c_2 e^{-imt} \left(1 + \frac{1}{r} (im + \frac{1}{6} m^2 r_i^2) - \frac{m^2 r^2}{6r_i} + \mathcal{O}(m^3) \right) \quad (3.21)$$

where $c_2 \approx \sqrt{\rho_i/2m^2}$.

In (3.20) note that the field amplitude near the horizon is enhanced by a factor $1 + m^2 r_i/2$ (an effect which was neglected in (2.21)). Also the terms quadratic in the mass, although they are still small compared to 1 since $kr_i = mvr_i = m\sqrt{r_i} < 1$, can dominate over the term linear in the mass.¹⁸ For the term linear in m to dominate all the way out to $r = r_i$ we require $mr_i^2 < 1$ or equivalently $mr_s < v^4$, which would put us back in regime I. In (3.21) the quadratic $m^2 r^2$ term can be understood as the expansion of a standing wave $\sim \frac{1}{kr} \sin kr$ to quadratic order in k . When $mr_s > v^4$ the

¹⁸In appendix B this corresponds to the fact that the expansion in powers of m involves both mr_s and $m\sqrt{rr_s}$.

standing wave starts to dominate over the im/r tail in the field profile. But the im/r tail is still important because the standing wave carries no flux. So energy transport into the black hole still comes from the im/r tail.

- III. As the mass increases further we enter a regime where $kr_i = mvr_i > 1$ and the field begins to oscillate. With the scaling $v^2 \sim 1/r_i$ this happens when $m \gtrsim v$, so we are not yet in the regime $m \gtrsim 1$ where the wave can easily fall into the black hole. Instead, it reflects off the potential and sets up a standing wave outside the black hole. Matching the solution (2.18) to spherical waves at $r > r_i$ gives

$$\phi(t, 1/m^2 < r < r_i) = \sqrt{\frac{\rho_i}{m^2}} \left(\frac{r_i}{r}\right)^{3/4} e^{-imt} \cos(2m\sqrt{r} - 3\pi/4), \quad (3.22)$$

$$\phi(t, r > r_i) = \sqrt{\frac{\rho_i}{m^2}} \frac{r_i}{r} e^{-imt} \cos(kr + m\sqrt{r_i} - 3\pi/4). \quad (3.23)$$

This matching makes the field and its first derivative continuous across r_i . To see this it is enough to recall that $\omega \approx m$ implies $k \approx m/\sqrt{r_i}$.

- IV. In regime IV, $m > 1$, the barrier around the black hole disappears and the wave is purely ingoing. Matching (2.17) to an ingoing spherical wave gives

$$\phi(t, 1 < r < r_i) = \sqrt{\frac{\rho_i}{2m^2}} \left(\frac{r_i}{r}\right)^{3/4} e^{-imt} e^{-2im\sqrt{r}}, \quad (3.24)$$

$$\phi(t, r > r_i) = \sqrt{\frac{\rho_i}{2m^2}} \frac{r_i}{r} e^{-imt} e^{-i(kr+m\sqrt{r_i})}. \quad (3.25)$$

As a quantity that can help us distinguish between these different behaviors we introduce

$$\alpha_i = \frac{|r\partial_r\phi|_{r=r_i}}{|\phi|_{r=r_i}}. \quad (3.26)$$

Thus, from the discussion above:

- I, II. for low masses, we expect $\alpha_i \approx 0$, reflecting a homogeneous field;
- III. once a standing wave develops, the field has nodes so α_i should have spikes;
- IV. once the wave is purely ingoing the spikes go away.

As a related quantity, we can spatially average α_i over an oscillation.¹⁹ This leads to

$$\langle \alpha_i \rangle \equiv \sqrt{\frac{\langle |r\partial_r\phi|^2 \rangle}{\langle |\phi|^2 \rangle}} = \sqrt{1 + \frac{k^2 r_i^2}{f_i^2}}. \quad (3.27)$$

The averaging smooths out the spikes, but it also throws out the phase coherence responsible for the homogeneous field at low mass. So at low mass we expect $\alpha_i \rightarrow 0$ but $\langle \alpha_i \rangle \rightarrow 1$. These behaviors can be seen in Fig. 7.

¹⁹To illustrate the averaging procedure, for ϕ in (3.6) we would define $\langle |\phi|^2 \rangle = \frac{1}{\tau^2} (|b_1|^2 + |b_2|^2)$.

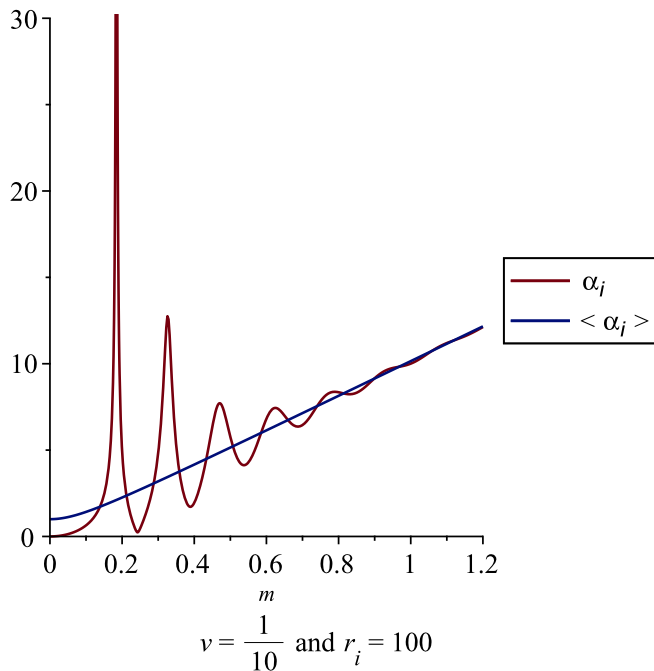


Figure 7: α_i and $\langle \alpha_i \rangle$ as a function of m .

3.4 Energy accretion rate

Finally we study the rate at which the black hole gains energy. In particular, we would like to compare the energy density in the scalar field at r_i ,

$$\rho_i \equiv T^{tt} = \frac{k^2 + 2m^2 f_i}{f_i^2} |\phi|^2 + |\partial_r \phi|^2 \quad \text{evaluated at } r = r_i, \quad (3.28)$$

with the flux of energy Φ_{horizon} entering the horizon—see Eq. (2.30). To this end, we introduce a quantity \mathcal{V} , defined by

$$\Phi_{\text{horizon}} = 4\pi r_i^2 \rho_i \mathcal{V}. \quad (3.29)$$

Since flux = area \times density \times velocity, we can interpret \mathcal{V} as the velocity at which the energy in the scalar field crosses r_i . As in the previous subsection, it is useful to average over spatial oscillations. This leads to the averaged energy density

$$\langle \rho_i \rangle = \frac{1}{f_i^2} \left(2m^2 f_i + 2k^2 + \frac{f_i^2}{r_i^2} \right) \frac{1}{r_i^2} \left(|b_1|^2 + |b_2|^2 \right), \quad (3.30)$$

which we can relate to the averaged velocity $\langle \mathcal{V} \rangle$ by

$$\Phi_{\text{horizon}} = 4\pi r_i^2 \langle \rho_i \rangle \langle \mathcal{V} \rangle. \quad (3.31)$$

We plot these quantities in Fig. 8, where we set $\omega = m$ and $r_i \gg 1$. As expected, averaging smooths out the spikes in \mathcal{V} . As can be seen in the figure, at large mass values $\mathcal{V} \rightarrow v$, while

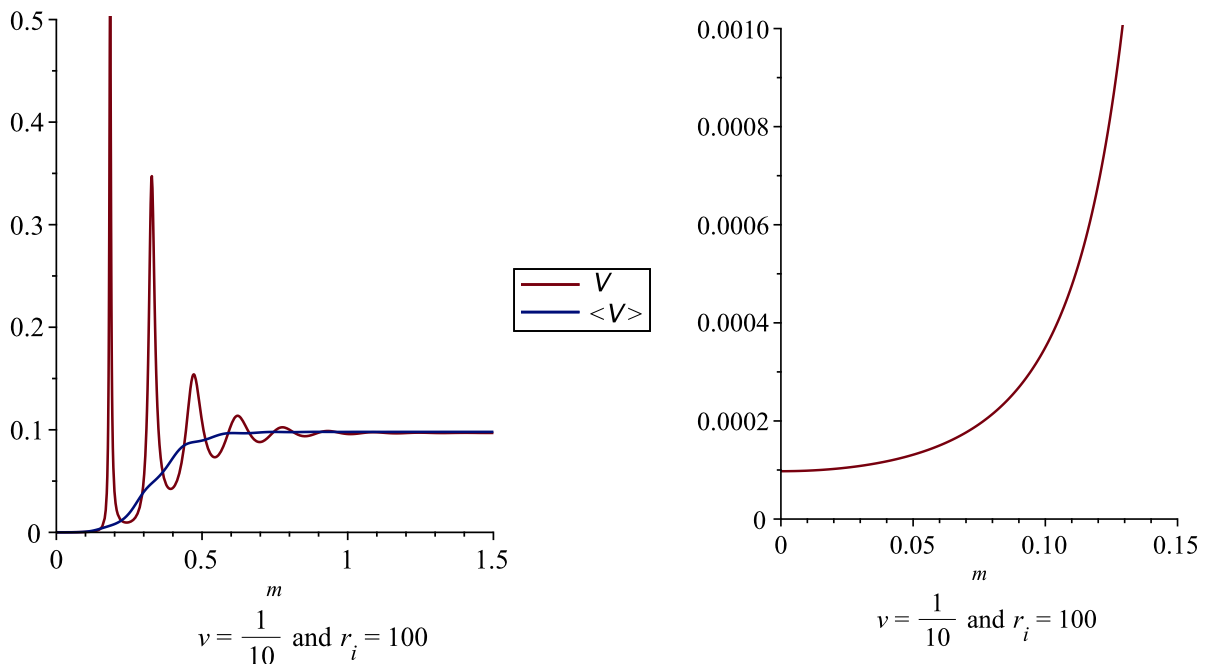


Figure 8: \mathcal{V} and $\langle \mathcal{V} \rangle$ as a function of m . The right panel zooms in on small mass. For small mass phase coherence is important so we don't show $\langle \mathcal{V} \rangle$.

for small masses $\mathcal{V} \rightarrow 1/r_i^2$. These results also follow from the expansions (3.9)-(3.12). Thus restoring the Schwarzschild radius r_s and the speed of light c we have

$$\text{large mass: } \Phi_{\text{horizon}} = 4\pi r_i^2 \rho_i v, \quad (3.32)$$

$$\text{small mass: } \Phi_{\text{horizon}} = 4\pi r_s^2 \rho_i c, \quad (3.33)$$

in agreement with (2.33) and (2.35). The first line is hardly a surprise—it is simply saying that energy moves across r_i with the velocity of the dark matter particles. To gain some intuition about the second line it is useful to switch to tortoise coordinates. In tortoise coordinates near the horizon the field is effectively massless and everything moves at the speed of light. The energy density in the tortoise coordinate is

$$\rho_* = \rho \frac{dr}{dr_*} = f^2 T^{tt} \quad (3.34)$$

which close to the horizon becomes $\rho_* \approx 2m^2|\phi|^2$. On the other hand for large r_i we have $\rho_i \approx 2m^2|\phi|^2$. For small mass, somewhat surprisingly, the field amplitude is the same near the horizon and at r_i . So ρ_i can be identified with the near-horizon energy density in tortoise coordinates, which accounts for (3.33).

4 Discussion

In this paper, we generalize a phenomenon first noted by Jacobson [1], that a time-dependent boundary condition for a scalar can endow a black hole with scalar hair. Our set-up is

regime	mass	$\phi(r_s \lesssim r < r_i)$
I	$mr_s < v^4$	$\sqrt{\frac{\rho_i}{2m^2}} \left(1 + \frac{imr_s^2}{r}\right)$
II	$v^4 < mr_s < v$	$\sqrt{\frac{\rho_i}{2m^2}} \left(1 + \frac{imr_s^2}{r} - \frac{1}{2}m^2rr_s\right)$
III	$v < mr_s < 1$	$\begin{cases} \sqrt{\frac{\pi\rho_i}{m^2}}(m^2r_i r_s)^{3/4} & r_s \lesssim r \lesssim 1/m^2r_s \\ \sqrt{\frac{\rho_i}{m^2}} \left(\frac{r_i}{r}\right)^{3/4} \cos(2m\sqrt{rr_s} - 3\pi/4) & 1/m^2r_s \lesssim r < r_i \end{cases}$
IV	$mr_s > 1$	$\sqrt{\frac{\rho_i}{2m^2}} \left(\frac{r_i}{r}\right)^{3/4} e^{-i2m\sqrt{rr_s}}$

Table 1: Field profile in different mass ranges. We set $\omega = m$ and denote the virial velocity by $v = \sqrt{r_s/r_i}$. For simplicity time dependence and some subleading terms have been suppressed.

motivated by (1) the fact that any astrophysical black hole is surrounded by dark matter, and (2) the notion that dark matter might be a scalar field, whose non-zero mass implies inevitable oscillations in time. The question is how much hair would be generated around the black hole.

To address this question, we revisit the Klein Gordon equation in a Schwarzschild background. This is an old subject with a vast literature (see e.g. [30, 31] for early papers). Our goal is to fill, as far as we know, a certain gap in the literature, working out the scalar profile around the black hole, as the scalar mass is systematically varied. Three assumptions are made in our computation: (1) that the angular momentum of the scalar is ignored, as is the spin of the black hole, (2) that the gravitational backreaction of the scalar is negligible, and (3) that the possible self-interaction of the scalar—for instance, if it were an axion—is unimportant.

We will address each of these points below, but let us first briefly summarize our findings. The scalar field has distinct profiles depending on the size of scalar mass m . There are four regimes, summarized in Fig. 1 and Table 1. Besides the scalar mass m , there are two additional scales in the problem: r_s the Schwarzschild radius of the black hole of course, and r_i the radius of sphere of impact, meaning at distances within r_i the geometry is dominated by the black hole. It is helpful to define a velocity scale $v \equiv \sqrt{r_s/r_i}$ which is the typical velocity dispersion at r_i . Regime I, the extreme low mass limit (or wave limit), is one where $mr_s < v^4$. The scalar field more or less oscillates with the same amplitude, from r_i all the way down to r_s . There is a $1/r$ component, whose coefficient can be identified as the scalar charge of the black hole, but it is very small. Regime II, where $v^4 < mr_s < v$, is very similar, with an additional (again small) linear r component. Regime III, with $v < mr_s < 1$, is perhaps the most interesting regime where one sees both particle-like and wave-like behavior. The scalar has a $1/r^{3/4}$ profile at large r which is characteristic of a particle (to be elaborated below), but also has a $\cos(2m\sqrt{rr_s} - 3\pi/4)$ modulation, characteristic of a standing wave. Regime IV, with $mr_s > 1$ i.e. the scalar Compton wavelength is smaller than the horizon size, is the particle limit with a $1/r^{3/4}$ profile but without the wave-like modulation. Observationally, it is probably challenging to measure the dark matter profile around an astrophysical black hole, but if it were possible, the profile can be used to deduce the dark matter mass. The standing wave nodes in regime III are particularly distinctive features to look for.

How do we understand the $1/r^{3/4}$ profile in the particle limit? Imagine a particle falling

towards the black hole from far away, it acquires a speed u that goes as $1/r^{1/2}$ by energy conservation.²⁰ In our computation, we are essentially looking for a stationary configuration of particles accreting onto the black hole. Such a stationary configuration would have an infalling flux that is independent of radius. In other words, we expect $4\pi r^2 \rho u$ to be independent of r . Thus, $\rho \propto 1/r^{3/2}$. Since $\rho \sim m^2 \phi^2$, the scalar field ϕ has a profile of $1/r^{3/4}$. This argument also explains the phase of ϕ in regime IV (see Eq. (2.17)): differentiating it with respect to r gives the particle momentum, and indeed the resulting $1/r^{1/2}$ is consistent with the velocity u we deduce by this simple argument. Phrased in this way, our black hole hair is in a sense fairly mundane: it is nothing other than a steady accretion flow of matter onto the black hole. The form of the flow changes as one dials the mass, from the particle limit to the wave limit.

It is worth noting that this argument is essentially what went into earlier discussions about a possible dark matter spike close to the black hole at the Galactic center, where the dark matter is assumed to be a heavy particle [51] (the density profile of $1/r^{3/2}$ can be seen in that context as originating from an initially flat one). Subsequent authors pointed out that the dark matter spike can be destroyed by dynamical processes as the seed black hole spiral to the center by dynamical friction [52]. The same caveats apply to our idealized computation as well, though for a sufficiently small dark matter particle mass, the resulting soliton that typically condenses at the center of galaxies [53] could have a stabilizing effect, a point we will come back to below.

Let us turn to the three assumptions outlined earlier. First, our computation is done largely assuming s-wave, or $l = 0$ (except in appendix A). This is a good approximation in the small mass limit. The angular momentum of a particle can be estimated as mvr_i , where v is defined earlier—the typical virial velocity at the radius of sphere of impact r_i i.e. $v = \sqrt{r_s/r_i}$. Thus, $mvr_i = mr_s/v$ which is less than unity as long as we are in regime I or II. For regime III and IV, ignoring angular momentum is no longer justified. However, at sufficiently large r —basically outside the angular momentum barrier which produces a turning point at $r \sim l^2/(m^2 r_s)$ —the $1/r^{3/4}$ profile remains valid (see appendix A for justification). Inside the angular momentum barrier, the scalar profile would depend on the angular momentum distribution of the scalar. There is of course also the angular momentum of the black hole itself, which we have ignored. For a spinning black hole, we expect our results to be applicable at a sufficiently large r , but there could be non-trivial effects, instability even, for instance the well known superradiance effect—we will return to this point below.

A second assumption we make is the absence of gravitational backreaction from the scalar. We can estimate the curvature produced by the dark matter scalar divided by the curvature sourced by the black hole, at around the horizon, by $16\pi Gr_s^2 \rho$. Here ρ is the dark matter density close to the black hole, which is at best $\rho_i (r_i/r_s)^{3/2}$ (the high mass limit), with ρ_i being the dark matter density at r_i far away from the black hole. Therefore:

$$16\pi Gr_s^2 \rho \lesssim 16\pi Gr_s^2 \rho_i \left(\frac{r_i}{r_s}\right)^{3/2} \sim 6 \times 10^{-13} \left(\frac{M_{\text{BH}}}{10^9 M_\odot}\right)^2 \left(\frac{\rho_i}{1 \text{ GeV/cm}^3}\right) \left(\frac{r_i/r_s}{10^6}\right)^{3/2}. \quad (4.1)$$

The value of $\rho_i \sim 1 \text{ GeV/cm}^3$ is about the dark matter density in the solar neighborhood. The gravitational backreaction is weak. Even boosting ρ_i by a few orders of magnitude for

²⁰For this argument, it does not matter a whole lot what precise velocity the particle originally had far away from the black hole. After some free fall towards the black hole, the particle's velocity would be dominated by the one generated by gravity, thus going as $1/r^{1/2}$.

a black hole in denser parts of the galaxy (or in denser galaxies) would not alter the basic smallness of the effect. See also [54] for estimates of related environmental effects around black hole binaries. A corollary of the weak gravitational backreaction is that the scalar hair would also be difficult to observe, since our primary way of deducing the existence of dark matter is via its gravitational effect.

A third assumption we make is that the scalar has negligible self-interaction. An appealing scalar dark matter candidate is the axion, or axion-like-particle. The axion is expected to have self-interaction, for instance a quartic term in the Lagrangian of the form $\mathcal{L}_{\text{quartic}} \sim (m/F)^2 \phi^4$, where F is the axion decay constant. One can estimate the importance of the self-interaction by taking the ratio of the quadratic mass term $\sim m^2 \phi^2$ and the quartic term, i.e. $\phi^2/F^2 \sim \rho/(m^2 F^2)$. Using the same reasoning as before, this is at best:

$$\begin{aligned} \frac{\rho}{m^2 F^2} &\lesssim \rho_i \left(\frac{r_i}{r_s}\right)^{3/2} \frac{1}{m^2 F^2} \\ &\sim 8 \times 10^{-7} \left(\frac{\rho_i}{1 \text{ GeV/cm}^3}\right) \left(\frac{r_i/r_s}{10^6}\right)^{3/2} \left(\frac{10^{-21} \text{ eV}}{m}\right)^2 \left(\frac{10^{17} \text{ GeV}}{F}\right)^2. \end{aligned} \quad (4.2)$$

Note that the upper limit makes use of the pile-up of the scalar close to the horizon, which applies only if the scalar mass is sufficiently large i.e. at least in regime III if not in regime IV i.e. $m \gtrsim 7 \times 10^{-23} \text{ eV} (10^9 M_\odot / M_{\text{BH}}) (10^6 / (r_i/r_s))^{1/2}$. It appears the self-interaction associated with an axion is also small, though the size depends the values for m and F . For the values chosen, the self-interaction effect is in fact a lot larger than the gravitational backreaction.

The above discussion suggests an interesting case to consider is one where the scalar mass is sufficiently small that a soliton is expected to condense at the center of halos [53], a possibility often referred to as fuzzy dark matter [19]. In such a case, the corresponding ρ_i can be much larger, *if* the black hole resides in the soliton. Let us investigate this in a concrete example: the supermassive black hole $M_{\text{BH}} \sim 6.5 \times 10^9 M_\odot$ in M87, recently imaged by the Event Horizon Telescope [48, 55, 56]. Its horizon size is equal to the Compton wavelength of a particle of mass $\sim 10^{-20} \text{ eV}$. From numerical simulations, the soliton mass is related to the halo mass by [53]:

$$M_{\text{soliton}} \sim 2 \times 10^9 M_\odot \left(\frac{10^{-22} \text{ eV}}{m}\right) \left(\frac{M_{\text{halo}}}{2 \times 10^{14} M_\odot}\right)^{1/3}, \quad (4.3)$$

where we adopt the mass of the Virgo cluster halo in which M87 resides [25]. The corresponding soliton radius is:

$$R_{\text{soliton}} \sim 5 \times 10^{15} \text{ km} \left(\frac{2 \times 10^9 M_\odot}{M_{\text{soliton}}}\right) \left(\frac{10^{-22} \text{ eV}}{m}\right)^2. \quad (4.4)$$

Using the results for the scalar pile-up in regime III and IV, we find that around the horizon, the dimensionless measure of the importance of self-interaction $\phi^2/F^2 \sim \rho/(m^2 F^2)$ is $\sim 10^{-7} - 10^{-3}$ for $m \sim 10^{-22} \text{ eV} - 10^{-20} \text{ eV}$.²¹ These numbers, while small, are potentially

²¹For these estimates, we use the soliton density for ρ_i and the soliton radius for r_i . Note that the soliton size and density should be altered by the presence of the black hole itself. Our estimates of the gravitational backreaction and the importance of self-interaction, based on the unaltered soliton size and density, are conservative: they are likely underestimates by about an order of magnitude. We thank Ben Church and Jerry Ostriker for discussions on this point.

important for superradiance considerations, appropriate in the context of a scalar Compton wavelength matching roughly the horizon size.²² Recall that the superradiance instability is rather slow: the growth rate is at best about 10^{-7} times the natural scale in the problem $1/r_s$ [58]. Self-interaction (or gravitational backreaction for that matter) introduces mixing between the superradiant mode and the scalar hair. The effect is weak but might be sufficient to have a non-negligible impact on superradiance. A detailed discussion is beyond the scope of this paper—for one thing, our computation needs to be generalized to a Kerr background—suffice to say the most interesting mixing comes from a possibly non-axisymmetric component of the hair (see [59] for discussions). It is also worth emphasizing that the supermassive black hole has the potential to swallow the soliton, as discussed in [25]. The accretion rate is $\sim 10^{-2} - 10^5 M_\odot/\text{year}$ for $m \sim 10^{-22} \text{ eV} - 10^{-20} \text{ eV}$, using the flux appropriate for regime III and IV.²³ There are several caveats, however: (1) the soliton-halo relation in Eq. (4.3) is an extrapolation from simulations of less massive halos; (2) the soliton might not have enough time to form (see discussion of relaxation time in [25]); (3) the impact of the black hole on soliton properties should be properly taken into account; (4) the black hole might not reside in the soliton. It would be interesting to perform simulations to map out these possibilities and understand the evolution of the soliton in more detail.

Let us end with a brief discussion of another possible scalar self-interaction. Instead of coming from a potential, such as in the case of the axion, the self-interaction could involve derivatives, such as in the case of superfluid dark matter [60]. In this case, the Lagrangian is generically a function $P(X)$ of the kinetic term $X \equiv -\frac{1}{2}\partial^\mu\phi\partial_\mu\phi$ and it is not hard to find solutions in the form $\phi(t, r) = t + \psi(r)$ that reduce to the Jacobson’s regular solution (1.2) near the horizon. In particular, for specific choices of the function $P(X)$, the field’s non-linearities can significantly change the scalar profile at distances of order of the Schwarzschild radius and enhance the estimate (4.1) by several orders of magnitude. These aspects will be analyzed in more details in a separate work.

Acknowledgments

We thank Pedro Ferreira, Austin Joyce, Alberto Nicolis, Riccardo Penco, Rachel Rosen, Enrico Trincherini and Michael Zlotnikov for discussions. We are grateful to Katy Clough, Pedro Ferreira and Macarena Lagos for sharing their manuscript with us. LH thanks Jerry Ostriker, Scott Tremaine and Edward Witten for earlier discussions on the black hole accretion of a scalar. DK thanks the Columbia University Center for Theoretical Physics for hospitality during this work. The work of DK is supported by U.S. National Science Foundation grant PHY-1820734. LS is supported by Simons Foundation Award Number 555117. LH and XL acknowledge support from NASA NXX16AB27G and DOE DE-SC011941. SW is supported in part by the Croucher Foundation.

²²See [57] for a recent discussion of constraints from the superradiance argument applied to the M87 black hole. For this argument, it is important to know the black hole spin, which is deduced primarily from the existence of a jet, rather than from the Event Horizon Telescope data. One main source of uncertainty on the spin is what fraction of the observed jet power could be powered by the accretion disk surrounding the black hole. We thank Eliot Quataert for discussions on this point.

²³The dimensionless number quantifying the importance of gravitational backreaction, $16\pi Gr_s^2\rho$, is related to the accretion rate. In all cases, it is negligible: at most 10^{-7} for $m \sim 10^{-20} \text{ eV}$.

A Scalar wave equation in Schwarzschild geometry

In this appendix we construct solutions to the Klein-Gordon equation for a massive scalar field in a Schwarzschild geometry in terms of the confluent Heun function, focusing in particular on solutions that are smooth across the future horizon. For generality we first set up the wave equation in a general static spherically-symmetric background, and in obtaining solutions we include angular momentum.

Given a general static, spherically symmetric background metric,

$$ds^2 = -f(r)dt^2 + \frac{1}{g(r)}dr^2 + r^2d\Omega^2, \quad (\text{A.1})$$

the ansatz $\phi(t, r, \hat{\Omega}) = e^{-i\omega t} \frac{R(r)}{r} Y_{l,n}(\hat{\Omega})$ allows to rewrite the wave equation

$$-\frac{1}{f} \partial_t^2 \phi + \frac{1}{r^2} \left(\frac{g}{f} \right)^{1/2} \partial_r \left(r^2 (fg)^{1/2} \partial_r \phi \right) - m^2 \phi = 0 \quad (\text{A.2})$$

as an effective radial Schrödinger equation

$$\left(-\partial_{r_*}^2 + V \right) R = \omega^2 R, \quad (\text{A.3})$$

where the tortoise coordinate and $R(r)$ are defined by

$$dr_* = \frac{dr}{(fg)^{1/2}}, \quad \phi(t, r) = e^{-i\omega t} \frac{R(r)}{r} \quad (\text{A.4})$$

and the potential is

$$V(r) = f \left(m^2 + \frac{l(l+1)}{r^2} \right) + \frac{1}{2r} \partial_r (fg). \quad (\text{A.5})$$

We now specialize to a Schwarzschild geometry and set

$$f(r) = g(r) = 1 - \frac{1}{r}. \quad (\text{A.6})$$

Thus, the tortoise coordinate becomes $r_* = r + \log(r-1)$ and the potential takes on the form

$$V(r) = \left(1 - \frac{1}{r} \right) \left(m^2 + \frac{l(l+1)}{r^2} + \frac{1}{r^3} \right). \quad (\text{A.7})$$

The general solution to (A.3) is given by confluent Heun functions [61, 62],

$$\begin{aligned} R(r) = & c_1 r(r-1)^{i\omega} e^{i\bar{k}r} \text{HeunC}(-2i\bar{k}, 2i\omega, 0, -\omega^2 - \bar{k}^2, \omega^2 + \bar{k}^2 - l(l+1), 1-r) \\ & + c_2 r(r-1)^{-i\omega} e^{-i\bar{k}r} \text{HeunC}(2i\bar{k}, -2i\omega, 0, -\omega^2 - \bar{k}^2, \omega^2 + \bar{k}^2 - l(l+1), 1-r). \end{aligned} \quad (\text{A.8})$$

Since we are interested in solutions that are smooth across the future horizon, we now examine the near-horizon behavior. As $r \rightarrow 1$ the confluent Heun functions approach 1, therefore

$$\phi(t, r) \approx c_1 e^{-i\omega(t-r_*)} e^{-i(\omega-\bar{k})} + c_2 e^{-i\omega(t+r_*)} e^{i(\omega-\bar{k})}. \quad (\text{A.9})$$

Imposing outgoing boundary conditions, as required by causality, is equivalent to setting $c_1 = 0$. This restricts us to the following solution which is smooth across the future horizon:

$$\phi(t, r) = c_2 e^{-i\omega t} (r-1)^{-i\omega} e^{-i\bar{k}r} \text{HeunC}(2i\bar{k}, -2i\omega, 0, -\omega^2 - \bar{k}^2, \omega^2 + \bar{k}^2 - l(l+1), 1-r). \quad (\text{A.10})$$

In order to systematically study large r asymptotics, we can first write (A.3) as

$$\left(\partial_r^2 + \bar{k}^2 + \frac{4\bar{k}^2 + 2m^2 - 2l(l+1) - 1}{2(r-1)} + \frac{2l(l+1) + 1}{2r} + \frac{4\bar{k}^2 + 4m^2 + 1}{4(r-1)^2} + \frac{1}{4r^2} \right) \left(R \sqrt{1 - \frac{1}{r}} \right) = 0. \quad (\text{A.11})$$

This gives the solution in terms in HeunC above. In the large r limit, one can look for asymptotic solution by expanding in $\frac{1}{r-1}$,

$$\left(\partial_r^2 + \bar{k}^2 + \frac{2\bar{k}^2 + m^2}{r-1} + \frac{\bar{k}^2 + m^2 - l(l+1)}{(r-1)^2} + \mathcal{O}\left(\frac{1}{(r-1)^3}\right) \right) \left(R \sqrt{1 - \frac{1}{r}} \right) = 0, \quad (\text{A.12})$$

where all the higher order terms do not depend on m and k . At this order the solution is given by the well-studied function ${}_1F_1$.

$$\begin{aligned} R(r) &\stackrel{r \gg 1}{\approx} \tilde{c}_1 \sqrt{r} (r-1)^{\frac{1}{2} \Delta_{\omega, l}} e^{-i\bar{k}r} {}_1F_1 \left(i\bar{k} + i \frac{m^2}{2\bar{k}} + \frac{1 + \Delta_{\omega, l}}{2}, 1 + \Delta_{\omega, l}, 2i\bar{k}(r-1) \right) \\ &\quad + \tilde{c}_2 \sqrt{r} (r-1)^{-\frac{1}{2} \Delta_{\omega, l}} e^{-i\bar{k}r} {}_1F_1 \left(i\bar{k} + i \frac{m^2}{2\bar{k}} + \frac{1 - \Delta_{\omega, l}}{2}, 1 - \Delta_{\omega, l}, 2i\bar{k}(r-1) \right), \\ \Delta_{\omega, l} &= i \sqrt{4\omega^2 - 4l(l+1) - 1}. \end{aligned} \quad (\text{A.13})$$

Therefore, from the asymptotic expansion of ${}_1F_1$ at large r , we have

$$\begin{aligned} \phi(t, r) &\approx c_3 e^{-i\omega t} \frac{1}{r} e^{i\bar{k}r + i(\bar{k} + \frac{m^2}{2\bar{k}}) \log(r-1)} (1 + \mathcal{O}(1/r)) \\ &\quad + c_4 e^{-i\omega t} \frac{1}{r} e^{-i\bar{k}r - i(\bar{k} + \frac{m^2}{2\bar{k}}) \log(r-1)} (1 + \mathcal{O}(1/r)). \end{aligned} \quad (\text{A.14})$$

These are the usual outgoing and ingoing spherical waves of flat space, with a logarithmic distortion due to the Newtonian tail of the potential. The coefficients c_3 and c_4 are given by the asymptotic expansion of ${}_1F_1$. The locations of the zeros of $c_4(\omega_n)$ are the approximate quasinormal modes frequencies. However, in general it is not known how \tilde{c}_1, \tilde{c}_2 are related to c_1, c_2 in this approximation. Only in the large mass regime, where ϕ is an ingoing wave everywhere, can we fix $\tilde{c}_2 \stackrel{m \gg 1}{\approx} c_2$ and $\tilde{c}_1 \stackrel{m \gg 1}{\approx} 0$. With angular momentum l , regime IV will be altered since there is an extra angular momentum barrier. One has to go to a larger mass, depending on l , such that the angular momentum barrier also vanishes. However the discussion below is general at large enough r .

Finally we consider the limit $\bar{k} \rightarrow 0$. In this limit the function ${}_1F_1$ reduces to ${}_0F_1$ which is related to a Bessel function. Therefore the $r \gg 1$ solution (A.13) in the large $m, \bar{k} = 0$ regime reduces to

$$\begin{aligned} R(r) &\stackrel{\bar{k}=0}{\approx} \tilde{c}_1 \Gamma(1 + \Delta_{m, l}) m^{-\Delta_{m, l}} \sqrt{r} J_{\Delta_{m, l}}(2m\sqrt{r-1}) \\ &\quad + \tilde{c}_2 \Gamma(1 - \Delta_{m, l}) m^{\Delta_{m, l}} \sqrt{r} J_{-\Delta_{m, l}}(2m\sqrt{r-1}), \end{aligned} \quad (\text{A.15})$$

where we have used the following identity,

$$\begin{aligned} & \lim_{\bar{k} \rightarrow 0} {}_1F_1 \left(i\bar{k} + i\frac{m^2}{2\bar{k}} + \frac{1 \pm \Delta_{\omega,l}}{2}, 1 \pm \Delta_{\omega,l}, 2i\bar{k}(r-1) \right) \\ &= \Gamma(1 \pm \Delta_{m,l}) m^{\pm \Delta_{m,l}} (r-1)^{\pm \frac{1}{2} \Delta_{m,l}} J_{\pm \Delta_{m,l}}(2m\sqrt{r-1}). \end{aligned}$$

If $m^2(r-1)$ is large the asymptotic expansion of the Bessel function gives

$$R(r) \sim r^{\frac{1}{4}} \cos(2m\sqrt{r-1} + \text{phase}). \quad (\text{A.16})$$

Therefore for $\bar{k} = 0$ the field profile $\phi(r)$ drops as $r^{-3/4}$ for all l in the region $r \gg \frac{1}{m^2 r_s}$. The discussion about regime IV in Sec. 2 is always valid while other regimes may behave differently for non-zero l .

B Asymptotics for $l = \bar{k} = 0$

In appendix A we obtained solutions to the wave equation in terms of confluent Heun functions. Here we study these solutions in more detail and obtain approximations valid in various regimes. After some preliminary definitions we specialize to fields with no angular momentum ($l = 0$) and frequency $\omega = m$ (equivalently $\bar{k} = 0$). For related discussion see [63].

The confluent Heun function, $\text{HeunC}(\alpha, \beta, \gamma, \delta, \eta; z)$, is defined by the following differential equation²⁴

$$\begin{aligned} & \text{HeunC}''(z) + \left(\alpha + \frac{1+\beta}{z} + \frac{1+\gamma}{z-1} \right) \text{HeunC}'(z) \\ & + \left(\frac{(\alpha(2+\beta+\gamma) + 2\delta)z + \beta(1+\gamma) - \alpha(1+\beta) + 2\eta + \gamma}{2z(z-1)} \right) \text{HeunC}(z) = 0, \end{aligned} \quad (\text{B.2})$$

with boundary conditions

$$\text{HeunC}(0) = 1, \quad \text{HeunC}'(0) = \frac{\beta(1+\gamma) - \alpha(1+\beta) + 2\eta + \gamma}{2(1+\beta)}. \quad (\text{B.3})$$

Its power series expansion around $z = 0$, $\text{HeunC}(z) = \sum_{n=0}^{\infty} a_n z^n$ for $|z| < 1$, obeys the following recurrence relation,

$$\begin{aligned} & P_n a_n = Q_n a_{n-1} + R_n a_{n-2}, \\ & P_n = n(n+\beta), \quad Q_n = (n-1)(n+\beta+\gamma-\alpha) + \frac{\beta(1+\gamma) - \alpha(1+\beta) + 2\eta + \gamma}{2}, \\ & R_n = (n-2)\alpha + \frac{1}{2}\alpha(\beta+\gamma+2) + \delta. \end{aligned} \quad (\text{B.4})$$

²⁴Note that in the literature e.g. in [61] the Heun function is written in terms of a different set of parameters, related to those appearing in (B.2), (B.3) by

$$\begin{aligned} & \text{“}\epsilon\text{”} = \alpha, \quad \text{“}\gamma\text{”} = 1 + \beta, \quad \text{“}\delta\text{”} = 1 + \gamma, \\ & \text{“}\alpha\text{”} = \frac{1}{2}\alpha(2 + \beta + \gamma), \quad \text{“}q\text{”} = \frac{1}{2}(-\beta(1 + \gamma) + \alpha(1 + \beta) - 2\eta - \gamma). \end{aligned} \quad (\text{B.1})$$

Carrying out this expansion for $\text{HeunC}(0, \beta, 0, \delta, -\delta, z)$, gathering terms to second order in β and first order in δ , and then re-summing the z -expansion we find that²⁵

$$\begin{aligned} \text{HeunC}(0, \beta, 0, \delta, -\delta, z) = & 1 - \frac{\beta}{2} \log(1-z) + \frac{\beta^2}{4} \left(\log(1-z) - \text{dilog}(1-z) \right) \\ & - \frac{\delta}{2} \left(z - \log(1-z) \right) + \dots \end{aligned} \quad (\text{B.5})$$

The Heun function of interest appears in (2.10). It involves the case $\beta = -2im$, $\delta = -m^2$, $z = 1 - r$ for which this expansion reads

$$\text{HeunC} = 1 + im \log r - \frac{1}{2} m^2 \left(r + 3 \log r - 2 \text{dilog} r - 1 \right) + \mathcal{O}(m^3), \quad (\text{B.6})$$

Before proceeding let us examine the expansion in powers of m more closely. The result (B.6) is valid up to quadratic order in the small mass m . Strictly speaking this expansion is valid as $m \rightarrow 0$ with all other parameters fixed. But other parameters in the problem – in particular the radius r – may be large, which means it is important to understand the nature of the expansion a little better. We start with the first non-trivial term. Restoring the Schwarzschild radius, and treating the log as $\mathcal{O}(1)$, the first non-trivial term is $\mathcal{O}(mr_s)$. It will be the dominant correction for sufficiently small mass (regime I in the paper). At second order the most important term for large radius $\sim m^2 r$. Restoring the Schwarzschild radius we see that, in addition to mr_s , another expansion parameter in the problem is $m\sqrt{rr_s}$. The second-order term should really be thought of as $\mathcal{O}((m\sqrt{rr_s})^2)$. Even when the m expansion is valid, the second-order term can dominate over the first-order term if the radius is large enough (this is regime II in the paper). Finally, when $m\sqrt{rr_s} > 1$ the expansion in powers of m breaks down. This is regimes III and IV in the paper.

To develop approximations valid in regimes III and IV let us return to the differential equation (A.3), which for $l = \bar{k} = 0$ reads

$$\left(-\partial_{r_*}^2 - \frac{m^2}{r} + \frac{1}{r^3} - \frac{1}{r^4} \right) R(r) = 0. \quad (\text{B.7})$$

First let us assume $mr_s < 1$ (regime III). Then we can divide the radial coordinate into two regions. In the “near-field” region ($r_s < r < 1/m$) the Newtonian potential $-m^2/r$ can be neglected compared to the relativistic corrections and the differential equation reduces to

$$\left(-\partial_{r_*}^2 + \frac{1}{r^3} - \frac{1}{r^4} \right) R(r) = 0. \quad (\text{B.8})$$

Rather than solve this equation, it is simpler to note that in the near-field region the expansion in powers of m is valid and to leading order (B.6) simply gives

$$\text{HeunC} \approx 1 \quad (\text{B.9})$$

(an approximation that is actually valid out to $r \sim 1/m^2$). From (2.10) this corresponds to

$$R \approx c_2 r e^{-im \log(r-1)}. \quad (\text{B.10})$$

²⁵Here $\text{dilog}(1-\chi) = \sum_{n=1}^{\infty} \frac{\chi^n}{n^2}$.

In the far-field region $1/m < r < \infty$, on the other hand, the Newtonian potential dominates and the differential equation reduces to

$$\left(-\partial_{r^*}^2 - \frac{m^2}{r}\right) R(r) = 0. \quad (\text{B.11})$$

This has a solution in terms of Bessel functions,

$$R(r) \approx \tilde{c}_1 \left(J_{2im}(2m\sqrt{r-1}) + i\sqrt{r-1} J_{1+2im}(2m\sqrt{r-1}) \right) + \tilde{c}_2 \left(J_{-2im}(2m\sqrt{r-1}) - i\sqrt{r-1} J_{1-2im}(2m\sqrt{r-1}) \right). \quad (\text{B.12})$$

It is straightforward to match the near- and far-field solutions (B.10), (B.12) at $mr \sim 1$. Requiring that the solutions and their radial derivatives are continuous gives, to leading order for small mr_s and assuming real c_2 ,

$$\tilde{c}_1 = \tilde{c}_2^* = \frac{c_2}{2im}. \quad (\text{B.13})$$

For $r < 1/m^2$ we adopt the approximation (B.10), while for $r > 1/m^2$ we expand the Bessel functions in (B.12) for large argument. This leads to

$$R(r) \approx \begin{cases} c_2 r e^{-im \log(r-1)} & 1 < r \ll 1/m^2 \\ \frac{c_2 r^{1/4}}{\sqrt{\pi} m^{3/2}} \cos\left(2m\sqrt{r} - \frac{3\pi}{4}\right) & r \gg 1/m^2 \end{cases} \quad (\text{B.14})$$

One could recast this result as an approximation for the Heun function, but this step is not necessary for our purposes. It is simpler to directly use $\phi(t, r) = e^{-imt} \frac{1}{r} R(r)$.

Finally, to study the behavior for $mr_s > 1$ (regime IV) we can proceed as follows. Note that when $mr_s > 1$ the Newtonian potential in (B.7) is dominant all the way down to the horizon at $r = 1$. This means the far-field solution (B.12) is valid all the way to the horizon, so we can impose the near-horizon in-going boundary condition (2.8) directly on the Bessel solution (B.12). This picks out a particular linear combination of Bessel functions and leads to

$$\text{HeunC}(0, -2im, 0, -m^2, m^2, 1-r) \approx \Gamma(1-2im) \frac{1}{r} \left(m\sqrt{r-1} \right)^{2im} \cdot \left(J_{-2im}(2m\sqrt{r-1}) - i\sqrt{r-1} J_{1-2im}(2m\sqrt{r-1}) \right). \quad (\text{B.15})$$

To study the right hand side for large m we use²⁶

$$J_\nu\left(\frac{\nu}{\cos\beta}\right) = \sqrt{\frac{2}{\pi\nu \tan\beta}} \left\{ \cos\left(\nu \tan\beta - \nu\beta - \frac{\pi}{4}\right) + \mathcal{O}(1/\nu) \right\}. \quad (\text{B.16})$$

Keeping the leading large- m behavior in (B.15) and expanding the amplitude (not the phase) for large r leads to the following approximation to the confluent Heun function

$$\text{HeunC} \approx \frac{1}{r^{3/4}} e^{-2im\left(\sqrt{r} - \log(\sqrt{r}+1) + \log 2 - 1\right)}. \quad (\text{B.17})$$

The approximations (B.6) and (B.17) are illustrated in Fig. 9.

²⁶This is known as approximation by tangents. It is valid for $\nu \rightarrow \infty$ with β fixed.

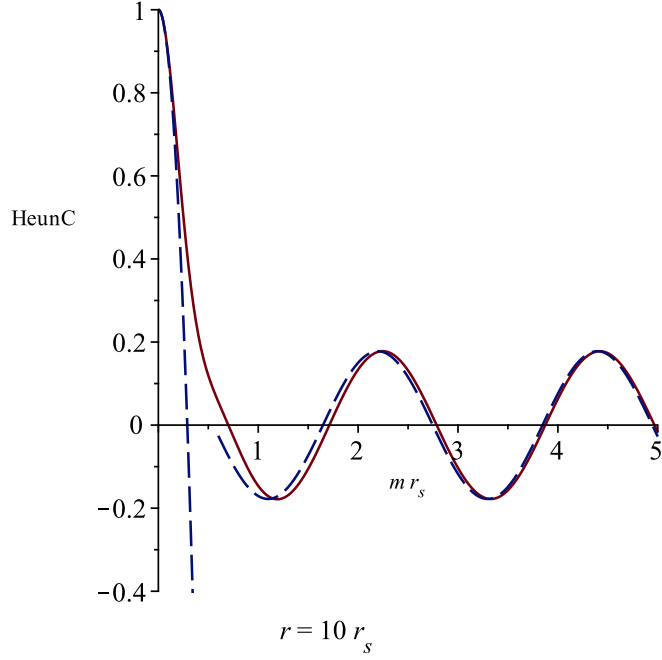


Figure 9: Real part of HeunC as a function of m for $r = 10$ (solid line). The approximations (B.6) and (B.17) are shown as dashed curves.

C Energy density and flux

In this section we obtain an expression for the rate at which energy is accreted by the black hole. We begin by considering a complex scalar field ϕ of mass m with action

$$S = \int d^4x \sqrt{-g} (-g^{\mu\nu} \partial_\mu \phi^* \partial_\nu \phi - m^2 \phi^* \phi) \quad (\text{C.1})$$

and stress tensor

$$T_{\mu\nu} = \partial_\mu \phi \partial_\nu \phi^* + \partial_\mu \phi^* \partial_\nu \phi + g_{\mu\nu} \mathcal{L}. \quad (\text{C.2})$$

Given the background geometry (A.1) and assuming a spherically symmetric ansatz for the scalar field, the non-vanishing components of the stress tensor are

$$T^{tt} = \frac{1}{f^2} (|\partial_t \phi|^2 + fg |\partial_r \phi|^2 + m^2 f |\phi|^2), \quad (\text{C.3})$$

$$T^{rt} = -\frac{g}{f} (\partial_t \phi \partial_r \phi^* + \partial_t \phi^* \partial_r \phi). \quad (\text{C.4})$$

The conservation equation for the stress tensor reads

$$\nabla_\mu T^{\mu\nu} = \frac{1}{\sqrt{-g}} \partial_\mu (\sqrt{-g} T^{\mu\nu}) + \Gamma_{\mu\lambda}^\nu T^{\mu\lambda} = 0. \quad (\text{C.5})$$

Then, setting $\nu = t$, we can massage the previous equation using $\Gamma_{tr}^t = \Gamma_{rt}^t = \frac{1}{2f} \frac{df}{dr}$ to get

$$\partial_t T^{tt} + \frac{1}{r^2} \left(\frac{g}{f}\right)^{1/2} \partial_r \left(r^2 \left(\frac{f}{g}\right)^{1/2} T^{rt}\right) + \frac{1}{f} \frac{df}{dr} T^{rt} = 0. \quad (\text{C.6})$$

Multiplying this by $r^2 f^{3/2}/g^{1/2}$ leads to the ordinary conservation law

$$\partial_t \left(r^2 \frac{f^{3/2}}{g^{1/2}} T^{tt} \right) + \partial_r \left(r^2 \frac{f^{3/2}}{g^{1/2}} T^{rt} \right) = 0. \quad (\text{C.7})$$

Finally, integrating over a spherical shell we find

$$dE = 4\pi r^2 \frac{f^{3/2}}{g^{1/2}} T^{tt} dr = (\text{energy between } r \text{ and } r + dr). \quad (\text{C.8})$$

Therefore, we can identify the energy flux (energy per unit time flowing inward) across a sphere of radius r as

$$\Phi = -4\pi r^2 \frac{f^{3/2}}{g^{1/2}} T^{rt}. \quad (\text{C.9})$$

Let us specialize to solutions that have definite frequency with respect to Killing time t and set

$$\phi(t, r) = e^{-i\omega t} \frac{1}{r} R(r). \quad (\text{C.10})$$

Then, the energy density becomes independent of time, while the energy flux is independent of both time and radius. In fact, the energy flux takes a simple form in terms of the tortoise coordinate $dr_* = dr/(fg)^{1/2}$:

$$\Phi = 4\pi i\omega (R^* \partial_{r_*} R - R \partial_{r_*} R^*), \quad (\text{C.11})$$

namely, it is proportional to the Wronskian, $W[R^*, R] = R^* \partial_{r_*} R - R \partial_{r_*} R^*$. Alternatively, it can also be thought of as being proportional to the probability flux in the effective Schrödinger equation (A.3). From either point of view Φ is independent of r as required by energy conservation. This means that we can evaluate the net energy flux using the near-horizon solution (A.9),

$$\Phi = 8\pi\omega^2 |c_2 e^{-i\bar{k}}|^2, \quad (\text{C.12})$$

where we retained the factor $e^{-i\bar{k}}$ to account for the possibility of imaginary \bar{k} .

The stress tensor for a real scalar field can be obtained simply by taking ϕ to be real and inserting a factor of 1/2. Thus for a real field

$$\begin{aligned} T^{tt} &= \frac{1}{2f^2} \left((\partial_t \phi)^2 + fg(\partial_r \phi)^2 + m^2 f \phi^2 \right), \\ T^{rt} &= -\frac{g}{f} \partial_t \phi \partial_r \phi. \end{aligned} \quad (\text{C.13})$$

References

- [1] T. Jacobson, “Primordial black hole evolution in tensor scalar cosmology,” [Phys. Rev. Lett.](#) **83** (1999) 2699–2702, [arXiv:astro-ph/9905303](#) [astro-ph].
- [2] J. D. Bekenstein, “Nonexistence of baryon number for static black holes,” [Phys. Rev.](#) **D5** (1972) 1239–1246.
- [3] T. P. Sotiriou and S.-Y. Zhou, “Black hole hair in generalized scalar-tensor gravity: An explicit example,” [Phys. Rev.](#) **D90** (2014) 124063, [arXiv:1408.1698](#) [gr-qc].

- [4] E. Babichev, C. Charmousis, A. Lehébel, and T. Moskalalets, “Black holes in a cubic Galileon universe,” [JCAP](#) **1609** (2016) no. 09, 011, [arXiv:1605.07438 \[gr-qc\]](#).
- [5] D. D. Doneva and S. S. Yazadjiev, “New Gauss-Bonnet Black Holes with Curvature-Induced Scalarization in Extended Scalar-Tensor Theories,” [Phys. Rev. Lett.](#) **120** (2018) no. 13, 131103, [arXiv:1711.01187 \[gr-qc\]](#).
- [6] H. O. Silva, J. Sakstein, L. Gualtieri, T. P. Sotiriou, and E. Berti, “Spontaneous scalarization of black holes and compact stars from a Gauss-Bonnet coupling,” [Phys. Rev. Lett.](#) **120** (2018) no. 13, 131104, [arXiv:1711.02080 \[gr-qc\]](#).
- [7] G. Antoniou, A. Bakopoulos, and P. Kanti, “Evasion of No-Hair Theorems and Novel Black-Hole Solutions in Gauss-Bonnet Theories,” [Phys. Rev. Lett.](#) **120** (2018) no. 13, 131102, [arXiv:1711.03390 \[hep-th\]](#).
- [8] G. Antoniou, A. Bakopoulos, and P. Kanti, “Black-Hole Solutions with Scalar Hair in Einstein-Scalar-Gauss-Bonnet Theories,” [Phys. Rev.](#) **D97** (2018) no. 8, 084037, [arXiv:1711.07431 \[hep-th\]](#).
- [9] C. F. B. Macedo, J. Sakstein, E. Berti, L. Gualtieri, H. O. Silva, and T. P. Sotiriou, “Self-interactions and Spontaneous Black Hole Scalarization,” [arXiv:1903.06784 \[gr-qc\]](#).
- [10] C. A. R. Herdeiro and E. Radu, “Asymptotically flat black holes with scalar hair: a review,” [Int. J. Mod. Phys.](#) **D24** (2015) no. 09, 1542014, [arXiv:1504.08209 \[gr-qc\]](#).
- [11] L. Hui and A. Nicolis, “No-Hair Theorem for the Galileon,” [Phys. Rev. Lett.](#) **110** (2013) 241104, [arXiv:1202.1296 \[hep-th\]](#).
- [12] M. R. Baldeschi, R. Ruffini, and G. B. Gelmini, “ON MASSIVE FERMIONS AND BOSONS IN GALACTIC HALOS,” [Phys. Lett.](#) **122B** (1983) 221–224.
- [13] M. S. Turner, “Coherent Scalar Field Oscillations in an Expanding Universe,” [Phys. Rev.](#) **D28** (1983) 1243.
- [14] W. H. Press, B. S. Ryden, and D. N. Spergel, “Single Mechanism for Generating Large Scale Structure and Providing Dark Missing Matter,” [Phys. Rev. Lett.](#) **64** (1990) 1084.
- [15] S.-J. Sin, “Late time cosmological phase transition and galactic halo as Bose liquid,” [Phys. Rev.](#) **D50** (1994) 3650–3654, [arXiv:hep-ph/9205208 \[hep-ph\]](#).
- [16] T. Matos and J. A. Nieto, “Topics on Kaluza-Klein theory,” [Rev. Mex. Fis.](#) **39** (1993) S81–S131.
- [17] P. J. E. Peebles, “Fluid dark matter,” [Astrophys. J.](#) **534** (2000) L127, [arXiv:astro-ph/0002495 \[astro-ph\]](#).
- [18] J. Goodman, “Repulsive dark matter,” [New Astron.](#) **5** (2000) 103, [arXiv:astro-ph/0003018 \[astro-ph\]](#).
- [19] W. Hu, R. Barkana, and A. Gruzinov, “Cold and fuzzy dark matter,” [Phys. Rev. Lett.](#) **85** (2000) 1158–1161, [arXiv:astro-ph/0003365 \[astro-ph\]](#).
- [20] J. Lesgourgues, A. Arbey, and P. Salati, “A light scalar field at the origin of galaxy rotation curves,” [New Astron. Rev.](#) **46** (2002) 791–799.
- [21] L. Amendola and R. Barbieri, “Dark matter from an ultra-light pseudo-Goldstone-boson,” [Phys. Lett.](#) **B642** (2006) 192–196, [arXiv:hep-ph/0509257 \[hep-ph\]](#).
- [22] P. Svrcek and E. Witten, “Axions In String Theory,” [JHEP](#) **06** (2006) 051, [arXiv:hep-th/0605206 \[hep-th\]](#).
- [23] A. Arvanitaki, S. Dimopoulos, S. Dubovsky, N. Kaloper, and J. March-Russell, “String Axiverse,” [Phys. Rev.](#) **D81** (2010) 123530, [arXiv:0905.4720 \[hep-th\]](#).

- [24] H.-Y. Schive, T. Chiueh, and T. Broadhurst, “Cosmic Structure as the Quantum Interference of a Coherent Dark Wave,” [*Nature Phys.* **10** \(2014\) 496–499](#), [arXiv:1406.6586 \[astro-ph.GA\]](#).
- [25] L. Hui, J. P. Ostriker, S. Tremaine, and E. Witten, “Ultralight scalars as cosmological dark matter,” [*Phys. Rev.* **D95** \(2017\) no. 4, 043541](#), [arXiv:1610.08297 \[astro-ph.CO\]](#).
- [26] R. Hlozek, D. Grin, D. J. E. Marsh, and P. G. Ferreira, “A search for ultralight axions using precision cosmological data,” [*Phys. Rev.* **D91** \(2015\) no. 10, 103512](#), [arXiv:1410.2896 \[astro-ph.CO\]](#).
- [27] P. Mocz and S. Succi, “Numerical solution of the nonlinear Schrödinger equation using smoothed-particle hydrodynamics,” [*Phys. Rev.* **E91** \(2015\) no. 5, 053304](#), [arXiv:1503.03869 \[physics.comp-ph\]](#).
- [28] M. Nori and M. Baldi, “AX-GADGET: a new code for cosmological simulations of Fuzzy Dark Matter and Axion models,” [*Mon. Not. Roy. Astron. Soc.* **478** \(2018\) no. 3, 3935–3951](#), [arXiv:1801.08144 \[astro-ph.CO\]](#).
- [29] J. Veltmaat, J. C. Niemeyer, and B. Schwabe, “Formation and structure of ultralight bosonic dark matter halos,” [*Phys. Rev.* **D98** \(2018\) no. 4, 043509](#), [arXiv:1804.09647 \[astro-ph.CO\]](#).
- [30] W. G. Unruh, “Absorption Cross-Section of Small Black Holes,” [*Phys. Rev.* **D14** \(1976\) 3251–3259](#).
- [31] S. L. Detweiler, “KLEIN-GORDON EQUATION AND ROTATING BLACK HOLES,” [*Phys. Rev.* **D22** \(1980\) 2323–2326](#).
- [32] P. P. Fiziev, “Exact solutions of Regge-Wheeler equation and quasi-normal modes of compact objects,” [*Class. Quant. Grav.* **23** \(2006\) 2447–2468](#), [arXiv:gr-qc/0509123 \[gr-qc\]](#).
- [33] P. P. Fiziev, “In the exact solutions of the Regge-Wheeler equation in the Schwarzschild black hole interior,” [arXiv:gr-qc/0603003 \[gr-qc\]](#).
- [34] V. B. Bezerra, H. S. Vieira, and A. A. Costa, “The Klein-Gordon equation in the spacetime of a charged and rotating black hole,” [*Class. Quant. Grav.* **31** \(2014\) no. 4, 045003](#), [arXiv:1312.4823 \[gr-qc\]](#).
- [35] H. S. Vieira, V. B. Bezerra, and C. R. Muniz, “Exact solutions of the Klein-Gordon equation in the Kerr-Newman background and Hawking radiation,” [*Annals Phys.* **350** \(2014\) 14–28](#), [arXiv:1401.5397 \[gr-qc\]](#).
- [36] R. A. Konoplya and A. Zhidenko, “Stability and quasinormal modes of the massive scalar field around Kerr black holes,” [*Phys. Rev.* **D73** \(2006\) 124040](#), [arXiv:gr-qc/0605013 \[gr-qc\]](#).
- [37] J. Barranco, A. Bernal, J. C. Degollado, A. Diez-Tejedor, M. Megevand, M. Alcubierre, D. Nunez, and O. Sarbach, “Schwarzschild black holes can wear scalar wigs,” [*Phys. Rev. Lett.* **109** \(2012\) 081102](#), [arXiv:1207.2153 \[gr-qc\]](#).
- [38] C. F. B. Macedo, P. Pani, V. Cardoso, and L. C. B. Crispino, “Into the lair: gravitational-wave signatures of dark matter,” [*Astrophys. J.* **774** \(2013\) 48](#), [arXiv:1302.2646 \[gr-qc\]](#).
- [39] M. W. Horbatsch and C. P. Burgess, “Cosmic Black-Hole Hair Growth and Quasar OJ287,” [*JCAP* **1205** \(2012\) 010](#), [arXiv:1111.4009 \[gr-qc\]](#).
- [40] Y. B. Zel’Dovich, “Amplification of Cylindrical Electromagnetic Waves Reflected from a Rotating Body,” [*Soviet Journal of Experimental and Theoretical Physics* **35** \(1972\) 1085](#).
- [41] A. A. Starobinskiĭ, “Amplification of waves during reflection from a rotating “black hole”,” [*Soviet Journal of Experimental and Theoretical Physics* **37** \(1973\) 28](#).
- [42] C. A. R. Herdeiro and E. Radu, “Kerr black holes with scalar hair,” [*Phys. Rev. Lett.* **112** \(2014\) 221101](#), [arXiv:1403.2757 \[gr-qc\]](#).

- [43] **LIGO Scientific, Virgo**, B. P. Abbott et al., “Observation of Gravitational Waves from a Binary Black Hole Merger,” [*Phys. Rev. Lett.* **116** \(2016\) no. 6, 061102](#), [arXiv:1602.03837 \[gr-qc\]](#).
- [44] P. Amaro-Seoane et al., “Low-frequency gravitational-wave science with eLISA/NGO,” [*Class. Quant. Grav.* **29** \(2012\) 124016](#), [arXiv:1202.0839 \[gr-qc\]](#).
- [45] P. Amaro-Seoane et al., “eLISA/NGO: Astrophysics and cosmology in the gravitational-wave millihertz regime,” [*GW Notes* **6** \(2013\) 4–110](#), [arXiv:1201.3621 \[astro-ph.CO\]](#).
- [46] G. Hobbs et al., “The international pulsar timing array project: using pulsars as a gravitational wave detector,” [*Class. Quant. Grav.* **27** \(2010\) 084013](#), [arXiv:0911.5206 \[astro-ph.SR\]](#).
- [47] **NANOGrav**, P. A. Gentile et al., “The NANOGrav 11 yr Data Set: Arecibo Observatory Polarimetry and Pulse Microcomponents,” [*Astrophys. J.* **862** \(2018\) no. 1, 47](#), [arXiv:1807.00708 \[astro-ph.HE\]](#).
- [48] **Event Horizon Telescope**, K. Akiyama et al., “First M87 Event Horizon Telescope Results. I. The Shadow of the Supermassive Black Hole,” [*Astrophys. J.* **875** \(2019\) no. 1, L1](#).
- [49] L. K. Wong, A.-C. Davis, and R. Gregory, “Effective field theory for black holes with induced scalar charges,” [arXiv:1903.07080 \[hep-th\]](#).
- [50] K. Clough, P. G. Ferreira, and M. Lagos, “On the growth of massive scalar hair around a Schwarzschild black hole,” [arXiv:1904.12783 \[gr-qc\]](#).
- [51] P. Gondolo and J. Silk, “Dark matter annihilation at the galactic center,” [*Phys. Rev. Lett.* **83** \(1999\) 1719–1722](#), [arXiv:astro-ph/9906391 \[astro-ph\]](#).
- [52] P. Ullio, H. Zhao, and M. Kamionkowski, “A Dark matter spike at the galactic center?,” [*Phys. Rev.* **D64** \(2001\) 043504](#), [arXiv:astro-ph/0101481 \[astro-ph\]](#).
- [53] H.-Y. Schive, M.-H. Liao, T.-P. Woo, S.-K. Wong, T. Chiueh, T. Broadhurst, and W. Y. P. Hwang, “Understanding the Core-Halo Relation of Quantum Wave Dark Matter from 3D Simulations,” [*Phys. Rev. Lett.* **113** \(2014\) no. 26, 261302](#), [arXiv:1407.7762 \[astro-ph.GA\]](#).
- [54] E. Barausse, V. Cardoso, and P. Pani, “Can environmental effects spoil precision gravitational-wave astrophysics?,” [*Phys. Rev.* **D89** \(2014\) no. 10, 104059](#), [arXiv:1404.7149 \[gr-qc\]](#).
- [55] **Event Horizon Telescope**, K. Akiyama et al., “First M87 Event Horizon Telescope Results. VI. The Shadow and Mass of the Central Black Hole,” [*Astrophys. J.* **875** \(2019\) no. 1, L6](#).
- [56] **Event Horizon Telescope**, K. Akiyama et al., “First M87 Event Horizon Telescope Results. V. Physical Origin of the Asymmetric Ring,” [*Astrophys. J.* **875** \(2019\) no. 1, L5](#).
- [57] H. Davoudiasl and P. B. Denton, “Ultra Light Boson Dark Matter and Event Horizon Telescope Observations of M87*,” [arXiv:1904.09242 \[astro-ph.CO\]](#).
- [58] S. R. Dolan, “Instability of the massive Klein-Gordon field on the Kerr spacetime,” [*Phys. Rev.* **D76** \(2007\) 084001](#), [arXiv:0705.2880 \[gr-qc\]](#).
- [59] A. Arvanitaki and S. Dubovsky, “Exploring the String Axiverse with Precision Black Hole Physics,” [*Phys. Rev.* **D83** \(2011\) 044026](#), [arXiv:1004.3558 \[hep-th\]](#).
- [60] L. Berezhiani and J. Khoury, “Theory of dark matter superfluidity,” [*Phys. Rev.* **D92** \(2015\) 103510](#), [arXiv:1507.01019 \[astro-ph.CO\]](#).
- [61] A. Ronveaux, ed., *Heun’s differential equations*. Oxford Science Publications. The Clarendon Press, Oxford University Press, New York, 1995. With contributions by F. M. Arscott, S. Yu. Slavyanov, D. Schmidt, G. Wolf, P. Maroni and A. Duval.
- [62] S. Slavjanov and L. Wolfgang, *Special Functions: A Unified Theory Based on Singularities*. Oxford Science Publications. Oxford University Press, 2000.

- [63] P. P. Fiziev, “Novel relations and new properties of confluent Heun’s functions and their derivatives of arbitrary order,” Journal of Physics A **43** (2009) no. 3, 035203, [arXiv:0904.0245 \[math-ph\]](#).